

QUASAR FEEDBACK AND THE ORIGIN OF RADIO EMISSION IN RADIO-QUIET QUASARS

NADIA L. ZAKAMSKA¹ AND JENNY E. GREENE²

Submitted to MNRAS, Feb 18 2014

ABSTRACT

We conduct kinematic analysis of the SDSS spectra of 568 obscured luminous quasars, with the emphasis on the kinematic structure of the [OIII] $\lambda 5007\text{\AA}$ emission line. [OIII] emission tends to show blueshifts and blue excess, which indicates that at least part of the narrow-line gas is undergoing an organized outflow. The velocity width containing 90% of line power ranges from 370 to 4780 km/sec, suggesting outflow velocities up to ~ 2000 km/sec. The velocity width of the [OIII] emission is positively correlated with the radio luminosity among the radio-quiet quasars. We propose that radio emission in radio-quiet quasars is due to relativistic particles accelerated in the shocks within the quasar-driven outflows; star formation in quasar hosts is insufficient to explain the observed radio emission. The median radio luminosity of the sample of $\nu L_\nu[1.4\text{GHz}] = 10^{40}$ erg/sec suggests a median kinetic luminosity of the quasar-driven wind of $L_{\text{wind}} = 3 \times 10^{44}$ erg/sec, or about 4% of the estimated median bolometric luminosity $L_{\text{bol}} = 8 \times 10^{45}$ erg/sec. Furthermore, the velocity width of [OIII] is positively correlated with mid-infrared luminosity, which suggests that outflows are ultimately driven by the radiative output of the quasar. As the outflow velocity increases, some emission lines characteristic of shocks in quasi-neutral medium increase as well, which we take as further evidence of quasar-driven winds propagating into the interstellar medium of the host galaxy. None of the kinematic components show correlations with the stellar velocity dispersions of the host galaxies, so there is no evidence that any of the gas in the narrow-line region of quasars is in dynamical equilibrium with the host galaxy. Quasar feedback appears to operate above the threshold luminosity of $L_{\text{bol}} \sim 3 \times 10^{45}$ erg/sec.

Subject headings: galaxies: evolution – galaxies: ISM – radio continuum: galaxies – quasars: emission lines

1. INTRODUCTION

Black hole feedback – the strong interaction between the energy output of supermassive black holes and their surrounding environments – is routinely invoked to explain the absence of overly luminous galaxies, the black hole vs. bulge correlations and the similarity of black hole accretion and star formation histories (Tabor & Binney 1993; Silk & Rees 1998; Springel et al. 2005; Hopkins et al. 2006). After years of intense observational effort, specific examples of black-hole-driven winds have now been identified using a variety of observational techniques, both at low and at high redshifts (Nesvadba et al. 2006; Arav et al. 2008; Nesvadba et al. 2008; Moe et al. 2009; Dunn et al. 2010; Alexander et al. 2010; Harrison et al. 2012). Nevertheless, the determination of the physical parameters of these outflows – including such basic parameters as the mass, the momentum and the kinetic energies they carry – remains challenging. Furthermore, it is far from clear how these outflows are launched near the black hole and established over the entire host galaxy.

Several years ago, we embarked on an observational program to determine whether radio-quiet, luminous quasars have observable effects on their galaxy-wide environment. One of our lines of investigations is to determine the extent and kinematics of the warm ($T \sim 10^4$ K)

ionized gas – the so-called narrow-line region of quasars. We simplify the observational task by looking at obscured quasars (Zakamska et al. 2003; Reyes et al. 2008) – those where the line of sight to the nucleus is blocked by intervening material, allowing us to study the distribution of matter in the galaxy unimpeded by the bright central source. We found strong evidence that ionized gas is extended over scales comparable to or exceeding that of the host galaxy; furthermore, it is kinematically disturbed and is not in equilibrium with the gravitational potential of the galaxy (Greene et al. 2009, 2011; Hainline et al. 2013).

More recently, we surveyed a sample of obscured radio-quiet quasars using a spectroscopic integral field unit (Liu et al. 2013a,b). We found extended ionized gas encompassing the entire host galaxy (median diameter of nebulae of 28 kpc), suggestive of wide-angle outflows, and determined kinetic energies of these outflows to be well in excess of 10^{44} erg/sec, with a median 2% conversion rate from the bolometric luminosity to the kinetic energy of warm ionized gas; more energy can be carried by other components. Furthermore, we identified several candidate objects where the wind has “broken out” of the denser regions of the galaxy and is now expanding into the intergalactic medium, sometimes in bubble-like structures (Greene et al. 2012; Liu et al. 2013b).

These observations demonstrate the presence of extended ionized gas in host galaxies of type 2 quasars, which is apparently out of dynamical equilibrium with the host galaxy and is likely in an outflow on the way out of the host. In this paper, we examine spectra of

¹ Department of Physics & Astronomy, Johns Hopkins University, Bloomberg Center, 3400 N. Charles St., Baltimore, MD 21218, USA

² Department of Astrophysical Sciences, Princeton University, Princeton, NJ 08544, USA

several hundred obscured quasars and we study the relationships between gas kinematics and other physical properties of these objects. In Section 2 we describe the sample selection, the dataset and the measurements. In Section 3, we conduct kinematic analysis of the optical emission lines. In Section 4 we discuss the relationships between multi-wavelength properties of quasars and kinematic measures of their ionized gas nebulae. In Section 5 we present composite spectra and discuss trends in weak emission lines. We present qualitative models for radio emission and emission lines in Section 6, and we summarize in Section 7.

We use a $h=0.7$, $\Omega_m=0.3$, $\Omega_\Lambda=0.7$ cosmology throughout this paper. SDSS uses vacuum wavelengths, but for consistency with previous literature we use air wavelengths in Angstroms to designate emission lines. Wavelengths are obtained from NIST (Kramida et al. 2013) and Atomic Line List³ and converted between air and vacuum as necessary using Morton (1991). Objects are identified as SDSS Jhhmm+ddmm, with full coordinates given in the catalog by Reyes et al. (2008). We use ‘1D’, ‘2D’ and ‘3D’ abbreviations for one-, two-, and three-dimensional values.

2. DATA AND MEASUREMENTS

2.1. Sample selection and host galaxy subtraction

Obscured quasar candidates studied here were selected from the spectroscopic data of the Sloan Digital Sky Survey (York et al. 2000) based on their emission line ratios and widths to be the luminous analogs of Seyfert 2 galaxies (Zakamska et al. 2003); the most recent sample contains 887 objects at $z < 0.8$ (Reyes et al. 2008). Infrared observations demonstrate that these sources have high bolometric luminosities (up to 10^{47} erg/sec, Zakamska et al. 2004, 2008; Liu et al. 2009). Chandra and XMM-Newton observations show that they contain luminous X-ray sources with large amounts of obscuration along the line of sight (Zakamska et al. 2004; Ptak et al. 2006; Vignali et al. 2010; Jia et al. 2012). HST imaging and ground-based spectropolarimetry display classical signatures of a buried broad-line active nucleus (Antonucci & Miller 1985; Zakamska et al. 2005, 2006). In other words, all follow-up observations thus far are consistent with these objects being luminous obscured quasars. Our estimate of the number density of these objects suggests that they are at least as common as unobscured quasars at the same redshifts and line luminosities (Reyes et al. 2008).

In this paper we examine the kinematic structure of narrow emission line gas in 568 objects (out of the entire sample of 887 by Reyes et al. 2008) selected to have [OIII] luminosities above $10^{8.5} L_\odot$. Their distribution in [OIII] luminosity / redshift space is shown in Figure 1. At the median redshift of the sample presented here $z = 0.397$, the SDSS fiber (3'' in diameter) covers the galaxies out to 8 kpc away from the center.

Ideally, we would like to measure the kinematics of the ionized gas relative to the host galaxy potential. The SDSS spectroscopic pipeline provides a high-quality redshift based on fits of observed spectra to a variety of library templates. In the cases of our objects, this pipeline

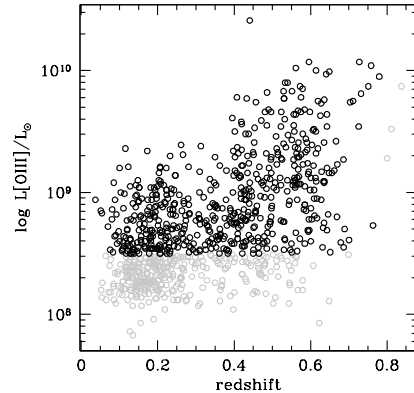


FIG. 1.— The distribution of the entire Reyes et al. (2008) sample of type 2 quasars in the redshift / [OIII] luminosity space (grey) and the 568 objects with kinematic analysis in this paper (black).

latches onto the strong emission lines, so the redshifts are affected by narrow line kinematics and may be offset from the redshifts of the host galaxies. Thus, our first step is to determine the host galaxy redshifts based on the absorption features produced in stellar photospheres.

Even though the quasars are obscured, the continuum from the host galaxy is very difficult to detect. One component of the continuum is due to the stars in the host galaxy. Furthermore, while the direct emission from the quasar is completely blocked in most cases, some quasar light reaches the observer after scattering off of the interstellar medium of the host galaxy and becomes an important continuum contribution at high quasar luminosities. Finally, in very luminous cases the Balmer continuum produced by free-bound transitions in the extended narrow emission line gas is also seen (Zakamska et al. 2005), and the emission lines tend to confuse the search for stellar features in the continuum.

We use the stellar velocity dispersion code described in detail in Greene & Ho (2006) and Greene et al. (2009) to model the host galaxy continuum and to establish the systemic velocity. The continuum of each quasar is modeled as the linear combination of three stellar models plus a power-law component to mimic a possible scattered light contribution (Zakamska et al. 2006; Liu et al. 2009). For templates, we use Bruzual & Charlot (2003) single stellar population models rather than individual stellar spectra.

We first shift the spectra into the approximate rest-frame by using the SDSS pipeline redshifts. Then we fit the continuum over the wavelength range 3680-5450 Å, allowing for the stellar models to have a velocity of up to 300 km/sec relative to the SDSS frame and to be broadened with a Gaussian function which represents the stellar velocity dispersion of the host. When the host galaxy is well detected, typical stellar absorption features visible in the spectra include Ca H+K, G-band, and Mg Ib lines. After this procedure, the entire host continuum is subtracted and the spectrum is shifted into the fine-tuned host galaxy frame.

We are able to identify some host galaxy features in 271 objects. In most of these cases, the absorption features are so weak that we do not consider the reported host velocity dispersions to be accurate. The greater

³ <http://www.pa.uky.edu/~peter/atomic/>

benefit of the host subtraction procedure is that in these 271 objects we can analyze narrow line kinematics relative to an accurately determined host frame. In the remaining objects we find no evidence for stellar features, so we subtract a featureless continuum. For the majority of objects, our workable wavelength range covers [OII] $\lambda\lambda 3726, 3729$, [OIII] $\lambda 5007$ and everything in between.

2.2. Fitting functions and non-parametric measurements

We aim to use non-parametric measures that do not depend strongly on the specific fitting procedure. We need robust measures or robust analogs of the first four moments of the line profile: typical average velocity, velocity dispersion, and the skewness and the kurtosis of the velocity distribution. We fit the profiles with one to three Gaussian components in velocity space, but in principle other fitting functions could be used. We assign no particular physical significance to any of the parameters of the individual components; rather, the goal is to obtain a noiseless approximation to the velocity profile.

We use relative change in reduced χ^2 values to evaluate which fit should be accepted; if adding an extra Gaussian component leads to a decrease in χ^2 of $<10\%$, we accept the fit with a smaller number of components. The single-Gaussian fit is accepted for 36 objects, two-Gaussian fit is accepted for 132 and the remaining 400 objects are fit with three Gaussians. Almost all objects that have high signal-to-noise observations have reduced χ^2 values that are too high to be statistically acceptable and thus would require either a larger number of components or different fitting functions to be fitted to statistical perfection. Fortunately, the non-parametric measures that we derive are rather robust: adding the third Gaussian component changes our second moment measure w_{80} by less than 10% in 83% of objects. Examples of line fits are shown in Figure 2. The objects selected for this figure have the top ten highest values of w_{80} (our analog of the velocity dispersion defined below).

Armed with fitting functions performed in velocity space $f(v)$, we construct the normalized cumulative velocity distribution $F(v) = \int_{-\infty}^v f(v')dv' / \int_{-\infty}^{+\infty} f(v')dv'$. Since the velocity profile is a noiseless non-negative function, $F(v)$ is strictly monotonically increasing. We then determine the velocities at which 5%, 25%, 50%, 75% and 95% of the line flux accumulates. The median velocity v_{50} is the solution of the equation $F(v) = 0.5$. The width comprising 90% of the flux is $w_{90} = v_{95} - v_{05}$, the width at 80% is $w_{80} = v_{90} - v_{10}$ and the width comprising 50% of the flux is $w_{50} = v_{75} - v_{25}$. All these values have dimensions of velocity (km/sec). For a Gaussian profile, the value w_{80} is very close to the conventionally used full width at half maximum ($w_{80} = 2.563\sigma = 1.088\text{FWHM}$; $w_{90} = 3.290\sigma$).

We can measure how asymmetric the velocity profile is relatively to the median velocity by computing a dimensionless relative asymmetry $R = ((v_{95} - v_{50}) - (v_{50} - v_{05})) / (v_{95} - v_{05})$. Negative values correspond to cases where the blue-shifted wing of the line extends to higher velocities than the red-shifted one, and positive values correspond to cases where the red-shifted wing dominates. This measure is a non-parametric ana-

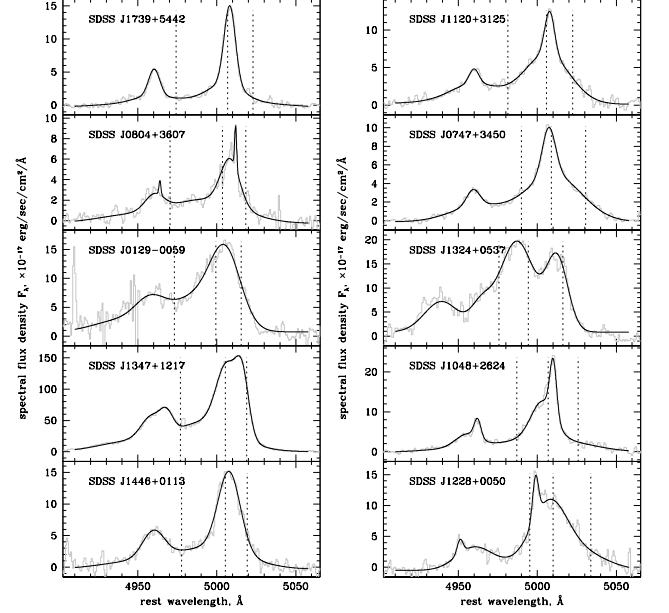


FIG. 2.— Spectra of the [OIII] $\lambda\lambda 4959, 5007$ doublet in the ten objects with the highest w_{80} values ($2314 \leq w_{80} \leq 2918$ km/sec), with their multi-Gaussian fits. The two lines in the doublet are fit simultaneously, under the assumption that the kinematic structure of both lines is the same and that the ratio of amplitudes is 0.337. Dashed lines show the positions of v_{10} , v_{50} and v_{90} .

log of skewness and is equal to 0 for any symmetric profile (including a single Gaussian). Furthermore, we can measure the prominence of the wings of the profile, or the non-parametric analog of the kurtosis, by computing $r_{9050} \equiv w_{90}/w_{50}$. For a Gaussian profile, this value is equal to 2.4389. Values higher than this indicate profiles with relatively more extended wings than a Gaussian function: for example, a Lorentzian profile $f(v) = 1/(\gamma^2 + v^2)$ (where γ is the measure of the profile width) has $r_{9050} = 6.3138$. Values lower than the Gaussian value indicate a profile with a stronger peak-to-wings ratio and are rarely encountered in our sample.

Finally, we compute the absolute asymmetry of the profile, which is $A = (\text{flux}(v > 0) - \text{flux}(v < 0)) / \text{total flux}$. In terms of the normalized cumulative velocity distribution, $A = 1 - 2F(0)$. This asymmetry is dimensionless and it is positive for profiles with more flux at red-shifted wavelengths than at blue-shifted wavelengths.

Values A and v_{50} critically depend on an accurate determination of the host galaxy redshift, because this is what we use to fix the $v = 0$ point. If no absorption features in the composite stellar light of the host are detected, the redshift can only be determined from the emission lines themselves, which renders the absolute velocity and skewness meaningless. Values of R , w_{90} , w_{80} , w_{50} , and r_{9050} include only differences between velocities and do not hinge on the accurate determination of the host velocity.

2.3. Robustness of non-parametric measures

In this section we evaluate the performance of the non-parametric measures. The theoretical advantage of the non-parametric measures is in their relative insensitivity to the fitting functions used. We test this assumption

by repeating all the fits using a set of one, two or three Lorentzian ($f(v) = 1/(\gamma^2 + v^2)$) profiles. The Lorentzian function has significantly more flux in the faint wings than does the Gaussian function, and this shape is in general not borne out in the observations of the line profiles in our sample. In general the quality of the fits with Lorentzian profiles is significantly poorer than of those with Gaussian profiles, and therefore all our final non-parametric measures are based on multi-Gaussian fitting as described in the previous subsection.

Nevertheless, we carry out the comparison between the non-parametric measures derived from the two methods. We find that both sets of fits yield nearly identical absolute asymmetries and median velocities v_{50} , which is not surprising because both these measures are most sensitive to the correct identification of the line centroid. All other measures (the widths, relative asymmetry and r_{9050}) are strongly correlated between the two sets of fits, but the specific values are systematically different. The line width w_{80} as measured from the Lorentzian fits is about 25% higher than that from the Gaussian fits; the relative asymmetry is significantly weaker as measured by Lorentzian profiles than the one measured by the Gaussian ones; and r_{9050} (Lorentzian) is approximately equal to r_{9050} (Gaussian)+2. All these differences are as expected from the fitting functions with different amount of power in the extended wings.

The conclusions we derive from this comparison are two-fold. First, since the multi-Lorentzian fits are not only statistically but also visibly inferior to the multi-Gaussian ones, the real systematic uncertainty on the $w_{80,90}$ – the key measurements discussed in this paper – is significantly smaller than the 25% difference between line widths calculated from these two methods. This is very encouraging. (For the majority of objects, w_{80} is accurate to 10% or better, as measured from the comparison of non-parametric measures derived from two-Gaussian and three-Gaussian fits.) Second, we confirm that the non-parametric measures are relatively robust: although the Lorentzian profiles do not yield statistically good fits, they nevertheless give reasonable estimates of the non-parametric measures.

We perform an additional test to determine the effect of the signal-to-noise ratio (S/N) of the spectra on our measurements. A narrow Gaussian emission line with a weak broad base observed with a high S/N is represented by two Gaussians in our multi-Gaussian fit, and its non-parametric measures include the power contributed by the weak broad base. On the contrary, if the same object is observed in a lower quality observation, the weak base is not necessarily recognized as such because the χ^2 of the two-Gaussian fit may be indistinguishable from the one-Gaussian one and thus the latter will be preferred.

We conduct the following Monte Carlo test to explore the effect of noise on our measurements. We take eight of the highest S/N objects in our catalog, four with $w_{80} > 1000$ km/sec and four with $w_{80} < 500$ km/sec. We then downgrade the quality of these spectra by adding progressively higher Gaussian random noise to the original (essentially noiseless) spectra and conduct all our multi-Gaussian and non-parametric measures in the manner identical to that used for real science observations. The results are shown in Figure 3. Both absolute asymmetry and v_{50} are relatively insensitive to the noise and do not

show systematic trends. The line width w_{80} does not depend on the noise for the four objects with relatively narrow ($w_{80} < 500$ km/sec) lines. But for the broad-line objects the measured w_{80} noticeably declines as the quality of observations worsens, reflecting the ‘missing broad base’ phenomenon. Measurements with peak S/N > 10 are relatively safe from this phenomenon: only one of the eight objects shows a noticeable decline of w_{80} at S/N $\lesssim 30$. The relative asymmetry and the kurtosis-like r_{9050} quickly drop to single-Gaussian values as the S/N decreases below 20 or so.

3. KINEMATIC ANALYSIS OF INTEGRATED SPECTRA

3.1. Outflow signatures

Interpreting the line-of-sight gas kinematic measurements in terms of physical 3D motions of the gas is highly non-trivial. This is true even when spatial information is available, for example, via integral-field observations (Liu et al. 2013b), but is even more so when we have to rely only on one spatially integrated spectrum. The reason is that if an object exhibits a spherically symmetric optically thin outflow, then its emission line profiles are symmetric and peaked at zero velocity, since there is a large amount of gas moving close to the plane of the sky. Therefore, there is simply no “smoking gun” outflow signature in the emission line profile of such a source. If an outflow has non-zero optical depth, then its presence can be inferred by its absorption of the background light at wavelengths blue-shifted relative to the quasar rest-frame, as happens in quasar absorption-line systems (Crenshaw et al. 2003; Arav et al. 2008), but this is not our case. Therefore, proving that a given line profile is due to gaseous outflow is often difficult and relies on indirect arguments (Liu et al. 2013b).

To investigate the relationship between the observed line-of-sight velocity dispersion of the lines and the typical outflow velocity, we consider for the moment a spherically symmetric outflow with a constant radial velocity v_0 . Because different streamlines have different inclinations to the line of sight, the observer sees a range of velocities – in this simplest case of the spatially integrated spectrum, the line profile is a top-hat between $-v_0$ and v_0 , so that $w_{80} = 1.6v_0$. In Liu et al. (2013b), we consider an outflow with a power-law luminosity density and calculate the velocity profiles in a spatially resolved observation, finding a typical $w_{80} \simeq 1.3v_0$ in the outer parts of the narrow line region. If a flow consists of clouds moving on average radially with velocity v_0 , but also having an isotropic velocity dispersion σ , then the observed w_{80} can be approximately calculated as $w_{80} \simeq \sqrt{(1.6v_0)^2 + (2.42\sigma)^2}$, as long as v_0 and σ are not too dissimilar.

Another simple case is a radial flow, in which at every point there are clouds with a range of radial velocities. As an example, we consider the results of the 2D simulations of quasar feedback by Novak et al. (2011), in which at every distance from the quasar the higher density regions (‘clouds’) have a wide distribution of radial velocities (G.Novak, private communication) which ranges from 0 to $\gtrsim 1000$ km/sec, with a median among all clouds of $v_0 = 220$ km/sec. We use the velocities of clouds straight from these simulations and several different luminosity density profiles to produce mock emission

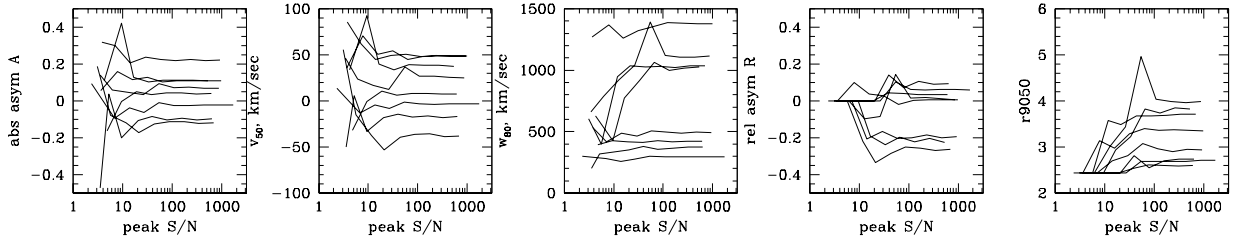


FIG. 3.— The dependence of non-parametric measures on the peak signal-to-noise ratio of the [OIII] emission line for eight spectra whose quality is progressively artificially downgraded by adding Gaussian random noise.

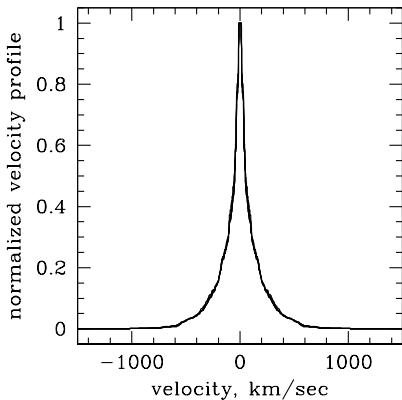


FIG. 4.— Mock emission line velocity profiles constructed from the cloud velocity distribution from Novak et al. (2011), using six different emissivity profiles (from linearly declining, to Gaussian, to flat, to centrally-tapered power law). All six curves are essentially on top of one another because the velocity distribution of the clouds hardly varies with the distance from the quasar in these simulations. The actual median radial velocity of the clouds is 220 km/sec, and we measure $w_{80} = 310$ km/sec and $w_{90} = 470$ km/sec for the simulated profile.

line profiles.

The resulting profiles are shown in Figure 4; they are insensitive to the adopted luminosity density profile because the velocity distribution of clouds does not change appreciably as a function of distance in these simulations. The profiles are peaked at zero velocity because there is a large population of clouds with small radial velocities, while the velocity dispersion of clouds is neglected in our calculations. If the clouds have an isotropic velocity dispersion which does not vary with distance, a more faithful profile can be obtained by convolving the profiles in Figure 4 with a Gaussian, which would make the profiles broader and less peaky. The measured velocity width of the profile is $w_{80} \simeq 1.4v_0$, similar to the scaling obtained in other simple cases, despite the broadness of the velocity distribution in this example.

To sum up, (i) there is no tell-tale outflow signature in an optically thin, spherically symmetric outflow; (ii) deviations from spherical symmetry (and moreover from axial symmetry) are required to produce asymmetric line profiles; and (iii) the velocity width of the emission line can be used to estimate the outflow velocity, $w_{80} \simeq (1.4 - 1.6) \times v_0$. The most natural way in which the symmetry may be expected to be broken is due to dust obscuration, either by dust embedded in the out-

flow itself or by dust concentrated in the galactic disk. In either case, the redshifted part is more affected by extinction, and thus excess blue-shifted emission is considered a sufficient indicator of an outflow (Heckman et al. 1981; De Robertis & Osterbrock 1984; Whittle 1985a; Wilson & Heckman 1985). In such case, the apparent w_{80} decreases typically by $\lesssim 30\%$ if the extinction is $\lesssim 2.5$ mag and concentrated in a disk (Liu et al. 2013b), reducing w_{80}/v_0 by the same amount. Thus for a given w_{80} , an asymmetric profile indicates a somewhat higher v_0 than a symmetric one.

Double-peaked profiles are expected in some geometries for a bi-conical outflow or more complex outflow kinematics (Crenshaw & Kraemer 2000), but can also be due to the rotation of the galaxy disk or two (or more) active nuclei in a merging system of galaxies, each illuminating its own narrow-line region. Distinguishing these possibilities usually requires follow-up observations at high spatial resolution, and the relative frequency of these scenarios remains a matter of debate (Comerford et al. 2009; Liu et al. 2010; Shen et al. 2010; Fu et al. 2012; Barrows et al. 2013; Blecha et al. 2013), but it appears that outflows dominate over dual active nuclei. It is likely that complex outflow kinematics is responsible for the majority of split-line profiles in our sample, and we conduct non-parametric kinematic measurements of such objects in the same way we do for the rest of the sample and include them in all our analyses.

3.2. Analysis of [OIII] kinematics

In Figure 5 we present the results of the non-parametric measurements of the [OIII] line in our sample of type 2 quasars. Both the relative asymmetry R and the absolute asymmetry A demonstrate slight preference for negative values, i.e., for blue excess. The blue asymmetries indicate that there is at least some outflow component in the [OIII]-emitting gas in type 2 quasars. The sample means and standard deviations for these values are $A = -0.03 \pm 0.15$ and $R = -0.08 \pm 0.15$. Line widths, relative asymmetries, kurtosis parameters and (to a lesser extent) median velocities are correlated with one another, in the sense that objects with broader lines also have a more pronounced blue excess (negative R), higher r_{9050} and more negative v_{50} (for the latter, the sample mean and standard deviation are -14 ± 75 km/sec).

From these correlations, a picture emerges in which the outflow component, or at least the component of the outflow which is more affected by the obscuration, tends to be broad. We further explore this notion in Figure

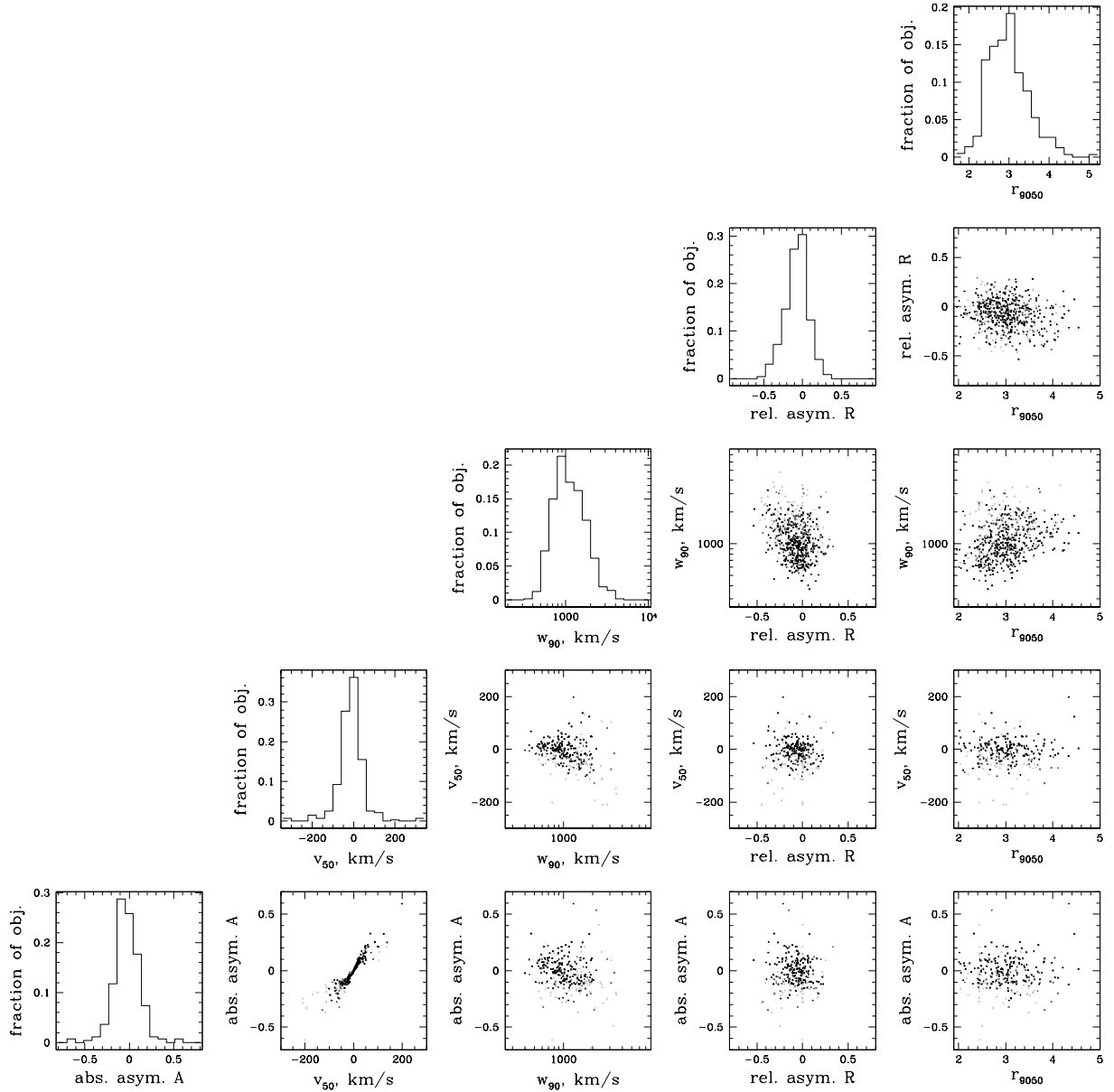


FIG. 5.— Distributions of non-parametric kinematic measures and their mutual relationships. Points are color-coded from light grey to dark grey by the peak signal-to-noise ratios (lightest have $S/N \lesssim 20$, grey have S/N from 20 to 50 and black have peak $S/N \gtrsim 50$). In all the plots involving absolute asymmetry A and median velocity v_{50} only points with reliable host redshifts are displayed since both these values critically depend on the host redshift determination.

6, where we split the line profiles into a ‘broad’ and a ‘narrow’ component. For objects with 2-Gaussian fits, the designation is straightforward, but the majority of objects require three Gaussians, in which case we pick the two most luminous ones and designate them ‘broad’ and ‘narrow’ according to their velocity dispersions. In Figure 6, we show that indeed the broader of the Gaussian components is the one that tends to be blue-shifted relative to the narrow ones. The narrow cores tend to be well-centered in the host galaxy frame; the mean and standard deviation of the centroids of the narrower Gaussian components is 3 ± 150 km/sec for the 271 objects with accurately determined host redshifts. On the con-

trary, the broader components tend to be slightly blue-shifted, both relative to the host galaxy frame (velocity centroid of -60 ± 210 km/sec in the 271 objects with accurate host redshifts) and relative to the narrow components ($v_{c,broad} - v_{c,narrow} = -90 \pm 270$ km/sec for the entire sample of 568 sources).

Because the narrow component is well-centered in the host frame, it is tempting to postulate that the narrow Gaussian component tends to be produced by gas in dynamical equilibrium with the host galaxy, e.g., in rotation in the galaxy disk, and is simply illuminated by the quasar, whereas the broad component is due to the outflow. However, we hesitate to make this inference,

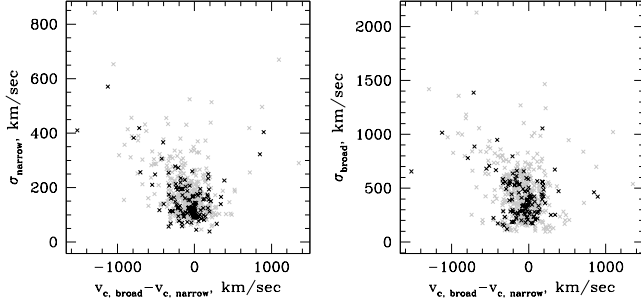


FIG. 6.— Velocity offset between the centroids of the broad component from the narrow component (black for profiles decomposed into two Gaussians, grey for the two Gaussians that dominate the flux in three-Gaussian decompositions). v_c is for the velocity centroids. Broad components tend to be blue-shifted relative to the narrow ones.

as there is no particular reason to assign any physical meaning to the individual parameters of the Gaussian components. We again draw a lesson here from Figure 4, where the mock emission line profile is due entirely to the outflowing clouds and can be decomposed into several Gaussian components, none of which correspond to the gas in rotation in the host galaxy.

We further test these ideas in Figure 7, where we show that neither the overall line width nor the width of the narrower Gaussian component show any correlation with the stellar velocity dispersion. Since even among the 271 objects where the host galaxy was detected many of the stellar velocity dispersions are rather poorly determined for the reasons discussed in Section 2.1, for this figure we use only the better determined stellar velocity dispersions from Greene et al. (2009). That the overall line width (left panel) shows no relationship with stellar velocity dispersion is not surprising if most of the line width arises due to the outflow. But the narrow cores do not appear to show any relationship with the stellar velocity dispersion either. As a result, it seems likely to us that virtually none of the [OIII]-emitting gas in type 2 quasars is in dynamical equilibrium with the host galaxy. This is in contrast to the situation in lower luminosity active galaxies in which [OIII] width strongly correlates with galaxy rotation and / or bulge velocity dispersion (Wilson & Heckman 1985; Whittle 1992; Nelson & Whittle 1996; Greene & Ho 2005). In such objects, it appears that the gas motions are in accord with the gravitational forces in the galaxy, and the gas is simply illuminated and photo-ionized by the active nucleus to produce the narrow-line region.

The relative shifts between the narrower and the broader components could arise if the narrow component is produced on all scales in the host galaxy, where it is less likely to suffer from strong extinction, whereas the broader component is produced closer to the nucleus, where it is more likely to be affected by extinction. This is consistent with an outflow that is driven close to the nucleus and then gradually slowed down by the interactions with the interstellar medium (Wagner et al. 2013). Furthermore, this picture is consistent with the apparent decline of the line width in the outer parts of the outflow seen in the integral field unit observations of type 2 quasars (Liu et al. 2013b), although the effect is small, with velocity width declining only by 3% per projected

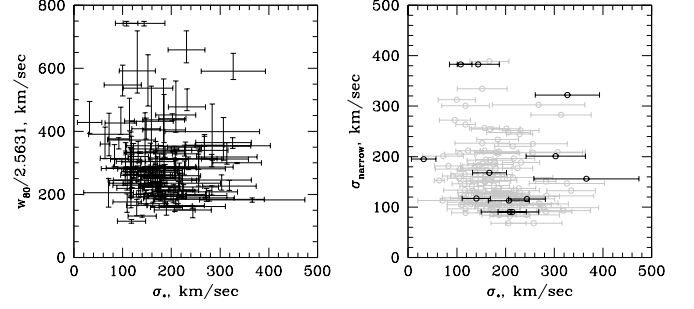


FIG. 7.— Taking just the objects with well-determined stellar velocity dispersions from Greene et al. (2009), we plot the overall width of the [OIII] emission line in the left panel and the dispersion of just the narrow component in the right panel as a function of the stellar velocity dispersion (grey points for the narrower of the two dominant components in a three-Gaussian fit, black points for the narrower of the two components in a two-Gaussian fit). The left panel is similar to Fig 7 of Greene et al. (2009) even though the exact non-parametric measures of dispersion used in that paper were defined differently.

kpc.

The sample mean and standard deviation of line width is $w_{90} = 1230 \pm 590$ km/sec, with a median of 1060 km/sec, minimum of 370 km/sec and maximum of 4780 km/sec ($w_{80} = 880 \pm 430$ km/sec, median 752 km/sec, min 280 km/sec, max 2918 km/sec), much higher than that of local Ultraluminous Infrared Galaxies (ULIRGs; median $w_{90} \simeq 800$ km/sec) and especially of those of them that do not have a powerful active nucleus in their center (median $w_{90} \simeq 600$ km/sec for pure starbursts, Hill & Zakamska 2013). For ULIRGs, the line widths and the outflow velocities strongly correlate with the power source (higher for active galaxies, lower for starbursts; Rupke & Veilleux 2013; Hill & Zakamska 2013), and the majority of the objects in our sample show line widths consistent with quasar-driven outflows, as expected. In Liu et al. (2013b), we estimated that for gas disks rotating in the potential of the most massive galaxies line widths do not exceed $w_{80} \simeq 600$ km/sec. Thus, the line-of-sight gas velocities that we see in our sample are too high to be confined even by the most massive galaxy potential, and this gas cannot be in dynamical equilibrium with the host galaxy.

The range of [OIII] luminosities in our sample is not all that large, with 90% of sources between $\log(L[\text{OIII}]/L_{\odot}) = 8.5$ and 9.5, with the remaining 10% sources spanning the higher decade in luminosity. There is some tendency of objects with more pronounced outflow signatures (higher width, higher r_{9050}) to have higher [OIII] luminosity (Spearman rank correlation coefficient $r_s \simeq 0.19$ for both relationships, probability of the null hypothesis of uncorrelated datasets $P_{\text{NH}} = 10^{-5}$), however, no correlations are seen between $L[\text{OIII}]$ and absolute asymmetry, relative asymmetry or median velocity. Furthermore, even though the correlations are nominally statistically significant we demonstrate below that the [OIII] luminosity is not the primary parameter driving the strength of outflow signatures. More likely, [OIII] luminosity is weakly correlated with another parameter (perhaps bolometric luminosity) that determines outflow kinematics, which leads to the correlations discussed above.

3.3. Fainter lines

We compare the kinematic structure of the brightest lines, [OIII] λ 5007, [OII] $\lambda\lambda$ 3726,3729, and H β . It has long been known that line kinematics often vary as a function of the ion ionization potential or the line critical density (Whittle 1985b). On the basis of largely anecdotal evidence, we previously established that in type 2 quasars with highly asymmetric or split-line [OIII] λ 5007 profiles the [OII] $\lambda\lambda$ 3726,3729 profiles seemed less complex (Zakamska et al. 2003). The difficulty of this analysis is illustrated in Figure 3: because [OIII] λ 5007 is by far the brightest line, it is much easier to miss a weak broad component in [OII] than in [OIII], giving the impression that the [OII] is narrower or lacks kinematic structures present in [OIII]. To remedy this problem, in what follows we use only the emission lines detected with peak S/N > 10 (about 230 objects), and we prefer S/N > 20 (about 140 objects).

We also need to take into account the doublet nature of [OII] $\lambda\lambda$ 3726,3729. Because the velocity spacing of the doublet (220 km/sec) is smaller than the typical line widths, we usually cannot deblend the two components. Thus observationally the most robust course of action is to measure the non-parametric width of the entire doublet which is then expected to be slightly higher than the width of a single (non-doublet) line with the same kinematic structure. To estimate the magnitude of this bias, we take the best multi-Gaussian fits for [OIII] λ 5007 for our entire sample and we simulate noiseless [OII] $\lambda\lambda$ 3726,3729 of the exact same kinematic structure assuming a 1:1, 1:1.2 and 1:1.4 line ratios within the doublet. We then refit the resulting [OII] profile, calculate its non-parametric widths without deblending and compare it with the ‘true’ input [OIII] non-parametric widths. We find the following relationships:

$$\begin{aligned} w_{50,\text{apparent}}[\text{OII}] &= \sqrt{w_{50,\text{true}}^2 + (175\text{km/sec})^2}; \\ w_{80,\text{apparent}}[\text{OII}] &= \sqrt{w_{80,\text{true}}^2 + (290\text{km/sec})^2}; \\ w_{90,\text{apparent}}[\text{OII}] &= \sqrt{w_{90,\text{true}}^2 + (340\text{km/sec})^2}. \end{aligned} \quad (1)$$

The accuracy of these fitting formulae is 7% (standard deviation). Now when we have the observed [OII] doublet, we need only measure its overall non-parametric measures and then invert equations (1) to correct for the doublet nature of the [OII] line. The magnitude of relative asymmetries and the kurtosis parameter r_{9050} of the simulated doublets are both slightly smaller than those of the input [OIII] λ 5007 profiles, as expected.

In Figure 8, we show the comparison between [OIII], [OII] and H β line widths. H β is slightly (8%) systematically narrower than [OIII] on average. Much of the difference is likely attributable to the signal-to-noise effect described in Section 2.3, since it is easier to miss a weak broad component in a noisy profile of H β than in the much higher S/N profile of [OIII]. There are only a few cases where the “by eye” examination of the [OIII] and H β profiles superposed on one another reveals that the [OIII] is genuinely significantly broader than the noisier H β (Figure 9).

In contrast, [OII] is noticeably narrower than [OIII] for high-width objects (Figure 8). The average doublet-

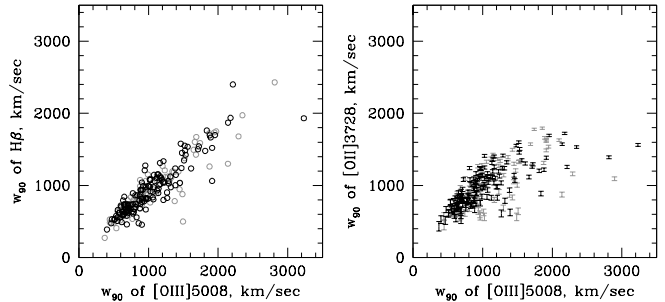


FIG. 8.— Comparison between non-parametric width measurements for [OIII] λ 5007, H β and [OII] $\lambda\lambda$ 3726,3729. In light grey are sources with estimated peak signal-to-noise of H β (left) and [OII] (right) between 10 and 20; in black are sources with S/N > 20. Because of the minimal S/N requirement, 223 sources appear in the left panel and 237 in the right. For [OII], the top of each bar corresponds to the non-parametric measure of the width of the entire non-deblended doublet, whereas the bottom of the bar includes the correction for the doublet splitting according to eq. (1).

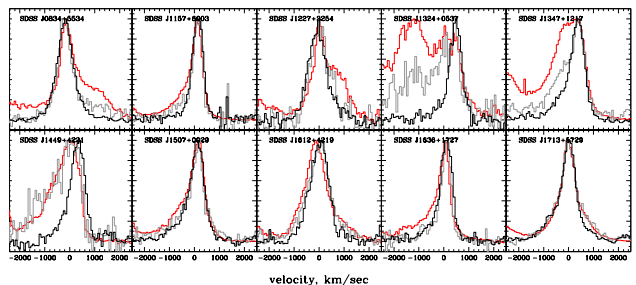


FIG. 9.— [OIII] (red), H β (grey) and [OII] (black) line profiles for the ten objects with the broadest [OIII] which also have S/N([OII]) > 10. The [OII] profiles are as observed, without any accounting for the doublet nature of the profile, although at these extreme line width the doublet splitting ~ 220 km/sec is not noticeable. Although both H β and [OII] are capable of showing asymmetries and complicated profile features, the kinematics of H β tends to be less extreme than that of [OIII], and of [OII] even less so, with H β typically seen in between [OIII] and [OII] profiles.

corrected width of [OII] over all 237 objects with peak S/N([OII]) > 10 is only 5% smaller than that of [OIII]; however, when we consider only objects with $w_{90}[\text{OIII}] > 1500$ km/sec, the difference in width increases to 27%. Overall while [OII] sometimes displays asymmetries and complicated profiles, it does not show the extremely broad features seen in [OIII], with H β demonstrating kinematics that are intermediate between [OII] and [OIII].

We conduct a similar examination of He II λ 4686 and [OIII] λ 4363 profiles, but only a handful of objects with S/N > 10 in these lines have relatively broad [OIII]. In these objects, [OIII] λ 5007, He II λ 4686 and [OIII] λ 4363 kinematic structures look, within the uncertainties, consistent with one another.

Line flux ratios involving [OIII] λ 5007, H β , [OII] $\lambda\lambda$ 3726,3729, He II λ 4686 and [OIII] λ 4363 (Osterbrock & Ferland 2006; Liu et al. 2013a) are diagnostic of the ionization state and temperature of the gas. We look for trends in these flux ratios as a function of all kinematic parameters and luminosity of [OIII]. Unfortunately, the variations in these line fluxes are subtle enough that high S/N values in the

fainter lines are required to measure their fluxes to the required accuracy. In particular, if it is the weak broad components that vary as a function of kinematics and / or luminosity, a S/N ratio of several tens in these lines would be required to detect these trends, as shown in Figure 3. As a result, we do not find any definitive trends in any of these ratios even when restricting the analysis to the small number of the highest signal-to-noise objects. Instead, we perform such measurements in Section 5 using composite spectra.

4. KINEMATICS AND MULTI-WAVELENGTH PROPERTIES

4.1. Kinematic indicators and radio emission

We cross-correlate our sample within $2''$ against the Faint Images of the Radio Sky at Twenty Centimeters (FIRST) survey at 1.4 GHz (Becker et al. 1995), which has typical 5σ sensitivity of ~ 1 mJy. When FIRST coverage is not available (about 6% of objects), we use the NRAO VLA Sky Survey (NVSS) survey at the same frequency (Condon et al. 1998), which has typical 5σ sensitivity of ~ 2.5 mJy. Out of the 568 objects in our sample, 386 have radio detections above the catalog sensitivity. For every source, we calculate the k-corrected radio luminosity at rest-frame 1.4 GHz,

$$\nu L_\nu = 4\pi D_L^2 \nu F_\nu (1+z)^{-1-\alpha}, \quad (2)$$

where $\nu = 1.4$ GHz, F_ν is the observed FIRST / NVSS flux (which corresponds to an intrinsically higher frequency in the rest-frame of the source), and α is the slope of the radio spectrum ($F_\nu \propto \nu^\alpha$), assumed to be -0.7 .

The exact shape of the radio luminosity function of active nuclei remains a topic of much debate, including whether there is a very broad distribution of intrinsic luminosities or whether there is a true dichotomy in this property (Kellermann et al. 1989; Xu et al. 1999; Ivezić et al. 2002; Jiang et al. 2007; Condon et al. 2013). In any case, the objects on the high end are traditionally called “radio-loud” and are sometimes very extended. In these cases, collimated relativistic jets propagate out to several hundred kpc from the host galaxy, and the radio emission of these sources is dominated by the lobes where the jet energy finally dissipates. The majority of our matches are weak (a few mJy) point sources at the $5''$ resolution of the FIRST survey. Since the optical broad-band emission of type 2 quasars is a poor proxy for their luminosity, we use the distribution of our sources in the [OIII] luminosity / radio luminosity plane to define the radio-loud / radio-quiet boundary (Xu et al. 1999) and find that about 10% qualify as classical radio-loud sources, and a similar fraction are significantly ($\gtrsim 10$ kpc) extended (Zakamska et al. 2004).

We find a strong correlation between the [OIII] line width and the radio luminosity (Figure 10). For nearby lower-luminosity active galaxies, similar relationships were previously reported by many authors (Heckman et al. 1981; Wilson & Heckman 1985; Whittle 1992; Nelson & Whittle 1996) and by Veilleux (1991b) whose sample is shown in Figure 10 for comparison. While there is a small tail of objects with very high radio luminosities, most of the correlation is due to the cloud of points at $\nu L_\nu[1.4\text{GHz}] = 10^{39} - 10^{41}$ erg/sec. Although these radio luminosities seem high by compar-

ison to those of the local active galaxies (e.g., the red points from the Veilleux 1991b sample), we need to keep in mind that the [OIII] luminosities of our type 2 quasars are at the extreme end of the luminosity distribution (right panel of Figure 10). Thus in the space of [OIII] vs radio luminosities (Xu et al. 1999) most of the type 2 quasars in our sample follow the radio-quiet, rather than the radio-loud, locus. Recently, Mullaney et al. (2013) also found a trend of increasing line width with radio luminosity using composite spectra of type 1 quasars with a wide range of [OIII] luminosities which overlaps with ours.

Taking all sources and radio upper limits at face value (i.e., assuming that the non-detections are close to the survey limit) yields a Spearman rank correlation coefficient of $r_s = 0.29$. Excluding radio-loud sources using their distribution in the [OIII]-radio plane (Zakamska et al. 2004) yields $r_s = 0.33$. If the non-detections are significantly below the survey limit, then the correlation is even stronger because there are hardly any non-detections on the high- w_{90} end of the diagram. In Section 6.1 we demonstrate that the radio fluxes of objects not detected by FIRST are likely within a factor of two of the FIRST survey limit. If we suppress all upper limits by a factor of two (but keep radio-loud sources in), the correlation has $r_s = 0.34$.

We also find an anti-correlation between radio luminosity and absolute asymmetry, $r_s = -0.37$, in the sense that objects with stronger blue asymmetry tend to have stronger radio emission. A similar relationship exists between radio luminosity and the median velocity v_{50} . In all these cases the null hypothesis (that the two datasets are uncorrelated) is rejected with $P_{\text{NH}} < 10^{-5}$, and these correlations are much stronger than those between kinematic measures and [OIII] luminosity reported in Section 3.2. Radio luminosity is not correlated with the other kinematic measures of outflow activity (relative asymmetry and kurtosis r_{9050}). For comparison, we also show the weaker trend between w_{90} and [OIII] luminosity reported in Section 3.2 in the right panel of Figure 10.

4.2. Kinematic indicators and infrared luminosity

We cross-correlate the entire sample of SDSS type 2 quasars (Reyes et al. 2008) against the Wide-field Infrared Survey Explorer (WISE) catalog within $6''$. Out of 887 objects in the catalog, 876 objects have matches in W1 ($3.6\mu\text{m}$) and W2 ($4.5\mu\text{m}$); 829 objects in W3 ($12\mu\text{m}$); and 773 objects in W4 ($22\mu\text{m}$) with signal-to-noise ratio above 2.5. The 11 objects without W1 matches are visually examined; in almost all cases there is an actual detection at the position of the quasar, but it is blended with a brighter nearby object and is thus not reported in the catalog. We interpolate between the WISE fluxes using piece-wise power-laws to calculate νL_ν at rest-frame 5 and $12\mu\text{m}$ and the index between these two, $\nu L_\nu \propto \lambda^\beta$ (higher index means redder spectral energy distribution). As the majority of the sources are well above the detection limit for the survey, the analysis of the WISE matches is not affected by non-detections to the same extent as the analysis of radio emission in the previous section.

The mid-infrared luminosities of type 2 quasars in our sample strongly correlate with their radio luminosities, [OIII] velocity widths and [OIII] luminosities (Figure 11).

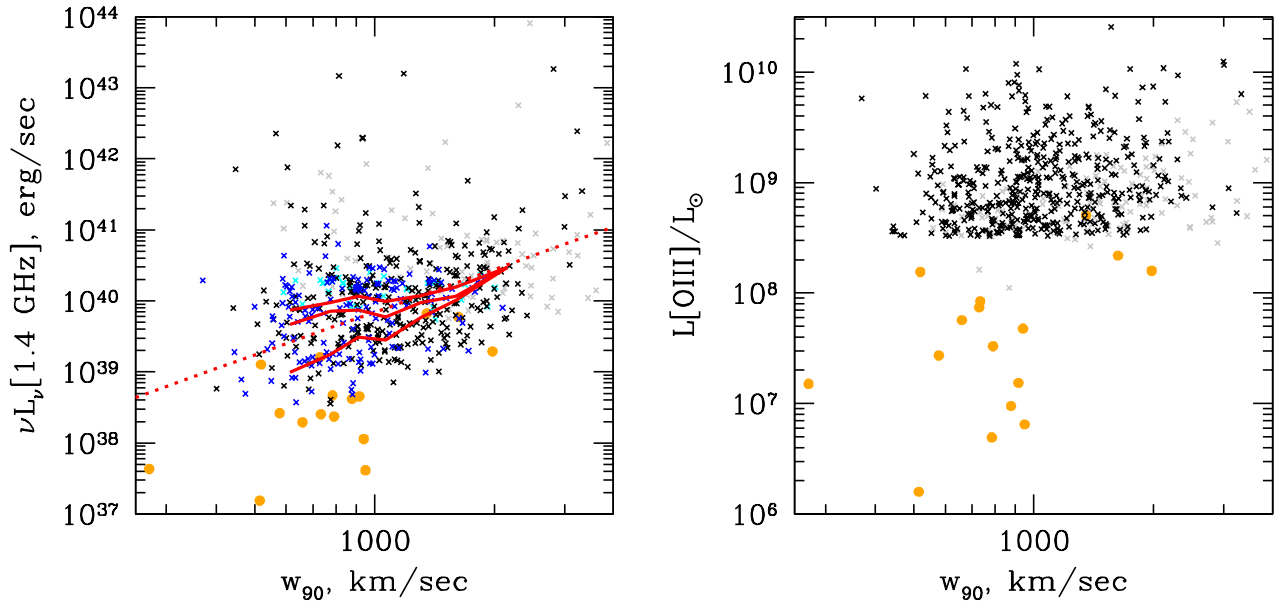


FIG. 10.— Left: Radio luminosities (k-corrected to the rest-frame 1.4 GHz) vs the velocity width w_{90} of the [OIII] emission. Crosses show 568 type 2 quasars in our kinematic analysis. Objects are color-coded by robustness of line fits (light grey, light blue for peak $S/N([OIII]) < 20$, black, dark blue for higher S/N) and by the status of radio matches (grey and black for radio detections, light blue and dark blue for radio upper limits). Filled orange circles show Seyfert galaxies from Veilleux (1991b); NVSS is used to determine the radio fluxes of these sources. The thick red lines show median radio luminosities in bins of line width. The top line assumes that radio non-detections are close to the limit of the survey, the bottom line assumes that non-detections are ten times fainter than the limit of the survey, and the middle line assumes that the non-detections are two times fainter than the limit of the survey. The dashed line shows $\nu L_\nu[1.4\text{GHz}] \propto w_{90}^2$; it is not a fit to the data. Right: There is a slight tendency for objects with broader [OIII] to also have higher [OIII] luminosity, but this correlation is much weaker than the relationship between w_{90} and radio luminosity.

The relationships between infrared luminosities, radio luminosities and [OIII] luminosities in low-luminosity active galaxies have been pointed out by many authors before, most recently by Rosario et al. (2013). For direct comparison with their work, we show the locus of normal starforming galaxies and the Rosario et al. (2013) line separating two branches of active nuclei in the left panel of Figure 11. Using νL_ν at $5\mu\text{m}$ instead results in similar relationships albeit with somewhat larger scatter.

Mid-infrared luminosities are correlated with all kinematic measures. The strongest correlation is with w_{90} ($r_s = 0.46$, $P_{\text{NH}} < 10^{-5}$), the second strongest with r_{9050} ($P_{\text{HN}} = 5 \times 10^{-4}$). There are also anti-correlations with absolute asymmetries, median velocities and relative asymmetries (all in the sense of higher mid-infrared luminosity in objects with stronger blueshifted excess), albeit at lower significance ($P_{\text{NH}} = 0.001 - 0.04$). There is a hint that the mid-infrared luminosity correlates positively with positive values of A , R and v_{50} , suggesting that either a strong blue asymmetry or a strong red asymmetry may be a sign of an outflow, although the latter objects are a small minority of our sample. Objects with higher w_{90} tend to have redder mid-infrared spectral energy distributions (higher β), with $r_s = 0.27$ and $P_{\text{NH}} < 10^{-5}$.

Rosario et al. (2013) point out that the Seyfert galaxies in their sample lie almost exactly on top of the locus of the star-forming galaxies in the radio / infrared diagrams. These authors conclude that only 15% of the infrared flux of these objects is due to the active nu-

cleus and that the correlation between infrared and radio fluxes seen among Seyfert galaxies is simply a reflection of the standard radio / infrared correlation due to star formation. Type 2 quasars appear to lie on the luminous extension of the locus of the star forming galaxies, and thus it is tempting to postulate that the same arguments apply in our sample, except the star formation rates of the host galaxies must be much higher than those seen in Seyferts by Rosario et al. (2013).

However, this explanation is unlikely to extend to the objects in our sample. The mid-infrared colors and fluxes of type 2 quasars at these luminosities are dominated by the quasar, not by the host galaxy (Lacy et al. 2004; Stern et al. 2005; Zakamska et al. 2008). Thus the strong correlation between radio and mid-infrared in this regime (and the excess of the radio emission over the amount seen in nearby star-forming galaxies) suggests that the radio emission in radio-quiet quasars is related to the quasar activity, not to the star formation in its host.

Our sample has 54 objects in common with Jia et al. (2012) who analyzed XMM-Newton and Chandra snapshots of a large sample of obscured quasars deriving their X-ray luminosities, spectral slopes and amount of intervening neutral gas absorption. These objects were either targeted by X-ray observatories or serendipitously lie in the fields of view of other targets. We do not find any correlations between any of the kinematic indicators and any of the X-ray spectral fitting parameters. In particular, there is no correlation between the optical line width and the absorption-corrected (intrinsic) X-ray luminosity. However, it must be kept in mind that the uncertain-

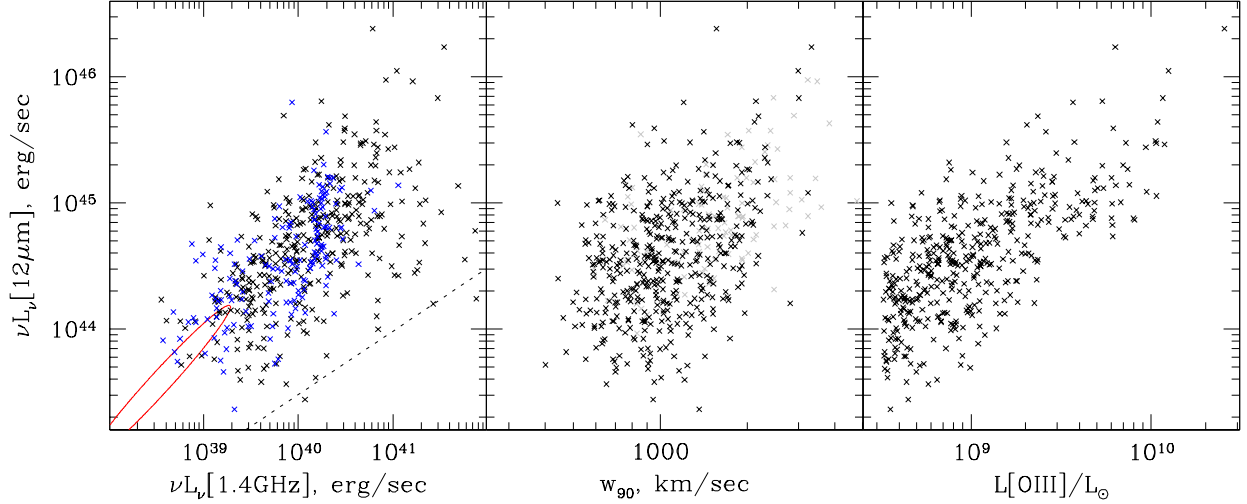


FIG. 11.— WISE monochromatic k-corrected luminosities as a function of radio luminosities (left), [OIII] velocity widths (middle) and [OIII] luminosities (right). In the left panel, the blue points are those with upper limits on radio fluxes, whereas the black points are radio detections. The red ellipse is the locus of star-forming galaxies from Rosario et al. (2013), and the dashed line is their separation line between infrared-bright (above the line) and infrared faint (below the line) branches of active nuclei. In the middle panel, grey points are for objects with peak $S/N[\text{OIII}] < 20$.

ties in the intrinsic X-ray luminosities tend to be rather high, especially because about half of the objects are Compton-thick, and deriving their intrinsic luminosities is particularly difficult. As a result, even the correlation between X-ray and mid-infrared luminosities – which are both supposed to be tracers of the bolometric luminosity – is rather weak ($P_{\text{NH}} \simeq 2\%$).

5. COMPOSITE SPECTRA

5.1. Constructing composites

To further test the trends we find in Sections 3 and 4 and to study weak emission features, we produce several sets of composite spectra. We choose a quantity that is easily measurable in every object (e.g., [OIII] line width in our first example) and bin the sample into five equal-size bins (114 objects) in this quantity. We then arithmetically average all host-subtracted spectra within each bin. This allows us to obtain high signal-to-noise composites while being able to tease out the dependencies on the chosen parameter. The composites produced in five bins of the [OIII] velocity width are presented in Figure 12 and the composites in five bins of [OIII] luminosity in Figure 13. Below we also discuss composites made in bins of infrared and radio luminosity, although these are not shown.

Even though the spectra are already host-subtracted, for accurate measurements of very weak lines we need a more accurate continuum subtraction. We select a dozen continuum-dominated wavelength intervals and spline-interpolate between them to produce the model of the continuum which is then subtracted from the composite spectrum. Continuum subtraction is the dominant source of systematic uncertainty in measuring the weak lines.

We then construct the velocity profile of the narrow-line region from the [OIII] $\lambda\lambda 4959, 5007$ lines and we use this profile to fit about 15 emission lines. Sev-

eral doublets which have wavelength separations that are too small to be resolved in our spectra are fitted with fixed ratios between the components, as follows: [OII] $\lambda\lambda 3726, 3729$ with a 1:1 ratio, [SII] $\lambda\lambda 4069, 4076$ with a 3:1 ratio (the doublet structure of this line is clearly visible in the lower w_{80} composites), and [NI] $\lambda\lambda 5198, 5200$ with a 1:1 ratio. For each emission feature, given the velocity profile from the [OIII] line, there is only one adjustable parameter – its amplitude. The fit is linear in all 15 amplitudes.

A few features are close blends: He I $\lambda 3889$ is blended with H ζ (8 \rightarrow 2 transition), and [NeIII] $\lambda 3968$ is blended with H ϵ (7 \rightarrow 2 transition). In both cases, the non-hydrogen emission makes a larger contribution to the blend, but not an overwhelmingly dominant one. To measure He I $\lambda 3889$ and [NeIII] $\lambda 3968$, we estimate the Balmer decrement from H β , H γ and H δ and use the derived extinction values to estimate H ϵ and H ζ , assuming Case B recombination (Osterbrock & Ferland 2006). We then subtract the extrapolated H ϵ and H ζ fluxes from the corresponding blends to obtain He I $\lambda 3889$ and [NeIII] $\lambda 3968$ fluxes separately.

The values of extinction we find using Balmer decrement and the Small Magellanic Cloud extinction curve from Weingartner & Draine (2001) are in the range $A_V = 1.0 - 1.5$ mag, in agreement with our previous estimates for type 2 quasars (Reyes et al. 2008) and with typical values in the literature for narrow-line regions of Seyfert galaxies (Bennert et al. 2006). Extinction values are higher ($A_V \simeq 1.5$ mag) for the two highest width composites than for the other ones ($A_V \simeq 1.0 - 1.1$ mag), somewhat reminiscent of the results by Veilleux (1991a) who finds higher extinction values for objects with stronger line asymmetries. As a function of luminosity, extinction decreases steeply and monotonically, from $A_V = 1.7$ mag to 0.9 mag. Because it is not clear that the extinction values derived from Balmer decre-

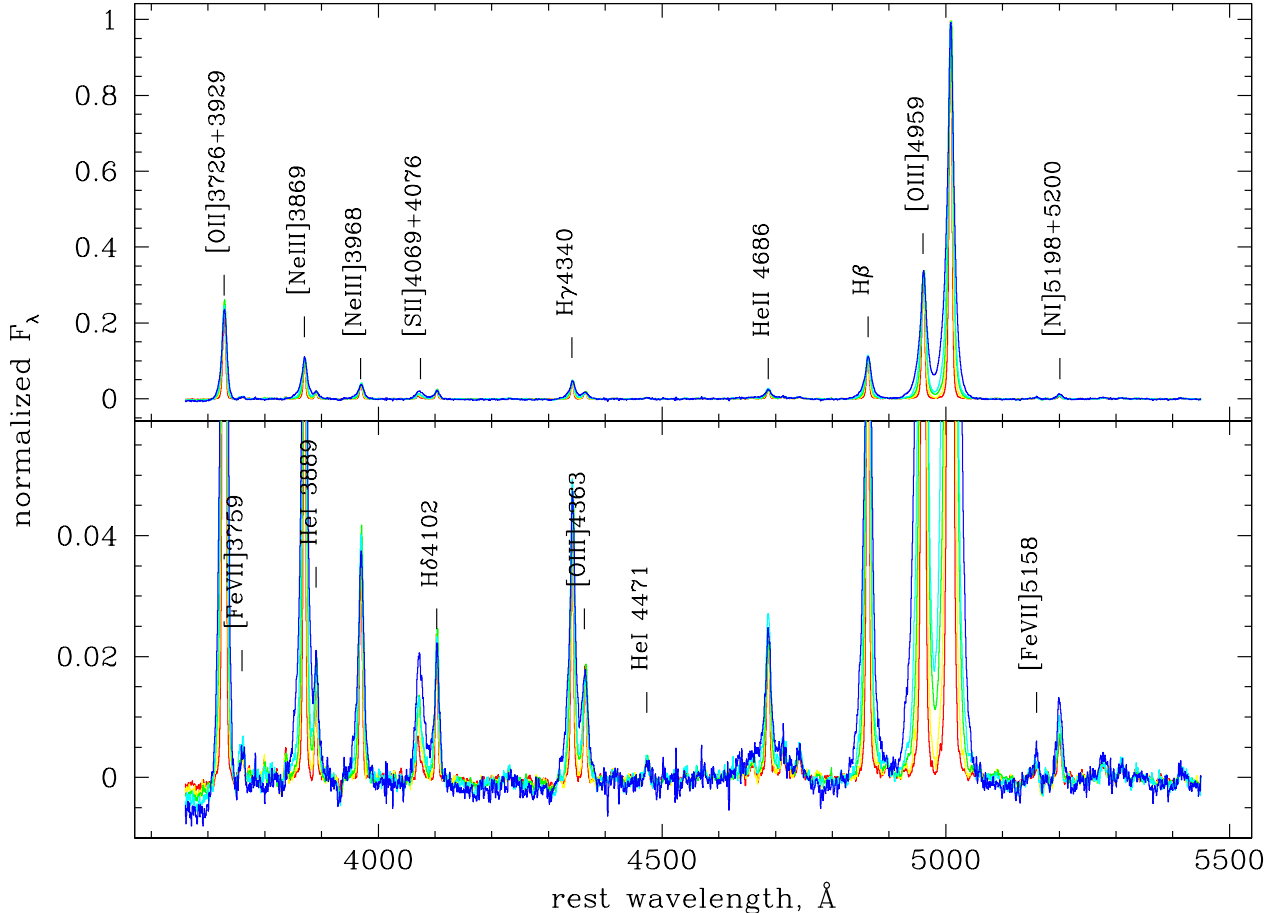


FIG. 12.— Composite in 5 bins of [OIII] w_{80} width (from red to blue w_{80} is increasing) normalized to the peak flux density of the [OIII] flux. Composite is straight-up error weighted mean in the host frame (whether or not the host subtraction is reported to be accurate). The bins are $w_{80} = 284 - 546$ km/sec, $546 - 673$ km/sec, $673 - 856$ km/sec, $856 - 1153$ km/sec, $1153 - 2918$ km/sec. Most of the line peaks line up from one composite to the next, but the peaks of [SII] $\lambda\lambda 4069, 4076$ and [NI] $\lambda\lambda 5198, 5200$ show a strong increase. [FeVII] $\lambda 5158$ appears to increase as well.

ments apply to all other emission features (which may originate in a different spatial region), we do not apply extinction correction to any measurements, unless explicitly stated otherwise.

The optimal composite-making practices depend on the goal of the composite (Vanden Berk et al. 2001; Lacy et al. 2013). The typical per-spectroscopic-pixel errors of the SDSS spectra are the result of the overall plate reductions and thus are not too dissimilar from one object to the next, so in an error-weighted average all weights would be roughly the same. Therefore we chose to use simple arithmetic averages to produce our composites (Lacy et al. 2013). It is encouraging that the [OIII]/[OII] line ratios measured from the composites ($\log[\text{OIII}]/[\text{OII}] = 0.67 - 0.74$, depending on [OIII] width) are consistent with the one measured from individual spectra (mean=median and sample standard deviation 0.70 ± 0.23) and [OIII] $\lambda 4959$ /[OIII] $\lambda 5007$ is within 1% of its theoretical value in all composites. This means that our composite-making procedure does a reasonable job of preserving line ratios, both for cases when the intrinsic distribution of the line ratio is very narrow (e.g., [OIII] $\lambda 4959$ /[OIII] $\lambda 5007$) and when it is fairly

broad (e.g., [OIII]/[OII]).

5.2. Wolf-Rayet features

One striking result is the appearance of a broad complex around He II $\lambda 4686$ in the composite with the highest w_{80} . This feature is somewhat reminiscent of the broad emission signatures of Wolf-Rayet stars (Brinchmann et al. 2008; Liu et al. 2009) – massive young stars which can radiatively drive outflows from their photospheres with velocities reaching 2000 km/sec. A detection (or lack thereof) of young stellar populations is of particular importance in our work, since supernova explosions are capable of driving powerful outflows. Thus, a significant star-forming population could be responsible for at least some of the outflow activity, and therefore this feature deserves particular scrutiny.

The emission-line region photo-ionized by the quasar produces a multitude of forbidden and recombination (‘nebular’) features in the wavelength range between 4600Å and 4750Å (Liu et al. 2009). The broad lines produced by the Wolf-Rayet stars at these wavelengths are N V $\lambda 4613$, N III $\lambda 4640$, C III/IV $\lambda 4650$, and He II $\lambda 4686$ (Brinchmann et al. 2008). Thus the challenge is

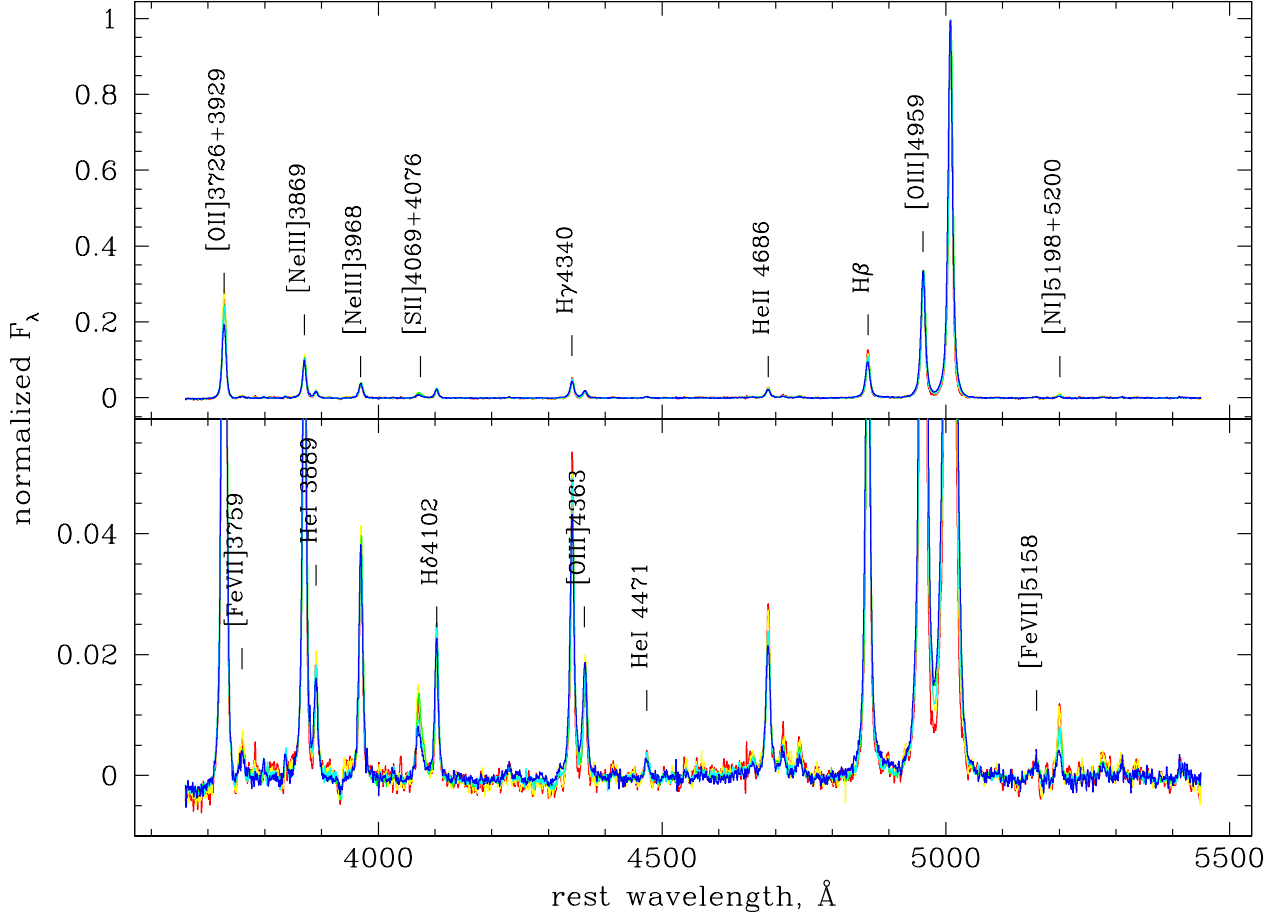


FIG. 13.— Composite in 5 bins of [OIII] luminosity (from red to blue $L[\text{OIII}]$ is increasing) normalized to the peak flux density of the [OIII] flux. The bins are $\log L[\text{OIII}]/L_{\odot} = 8.50 - 8.61, 8.61 - 8.78, 8.78 - 8.97, 8.97 - 9.23, 9.23 - 10.41$. Many of the line peaks decrease in the red \rightarrow blue sequence, but the line widths do not vary drastically, reflecting the weakness of the relationship between [OIII] luminosities and widths.

to disentangle the two sets, made even more difficult by the fact that at the high velocities of the “narrow” lines in our highest w_{80} objects the velocities in the quasar-ionized set are not dissimilar from the velocities in the Wolf-Rayet set.

In Figure 14 we zoom in on the wavelength range of interest. We find that only four nebular emission features ([Fe III] $\lambda 4658$, He II $\lambda 4686$, [Ar IV] $\lambda 4711$ and [Ar IV] $\lambda 4740$) are sufficient to explain most of the observed flux. For each composite, we assume that these four features are associated with the narrow-line region of the quasar and have the same kinematic structure as H β . We take the H β velocity profile from the same composite and we adjust its amplitude to fit each of these four features. We see no evidence that the relative fluxes of the four lines vary from one composite to the next; thus the models shown in Figure 14 have [Fe III]/He II fixed at 0.15 and each [Ar IV]/He II fixed at 0.20, making it essentially a one-parameter fit (the overall ratio of He II to H β). No broad component in He II is required to produce an adequate fit. There is some evidence in the last composite of some emission filling in between the two argon features, possibly due to [Ne IV] $\lambda 4725$.

Although most of the “broad” feature turns out to be

due to a superposition of relatively broad nebular lines, in the last panel we see excess emission centered at around 4640 Å. This is close to the wavelength of one of the more prominent Wolf-Rayet features, N III $\lambda 4640$. To estimate the flux of this feature, we model it using the same H β velocity profile (although in this case there is no particular physical reason to do so, since the N III line is expected to reflect the kinematics of the stellar winds, rather than be produced in the extended low-density medium of the host galaxy and reflect the kinematics of quasar-ionized gas). We find a reasonable fit with N III/He II=0.15, but we rather doubt the identification of this feature as N III associated with the Wolf-Rayet stars in the host galaxy. The feature is noisy and is somewhat offset to the blue from the nominal expected centroid. When all spectra are coadded together into a single composite, the evidence for N III disappears.

We assume for the moment that the N III feature is in fact detected and estimate its median luminosity. To this end, we use the observed N III / [OIII] ratios in the composite and the median [OIII] luminosity of the objects in the composite $\log L[\text{OIII}]/L_{\odot} = 8.91$ to find $L(\text{N III}) \simeq 3 \times 10^6 L_{\odot}$. We then use N III fluxes and starburst models from Schaerer et al. (1999) and Leitherer et al.

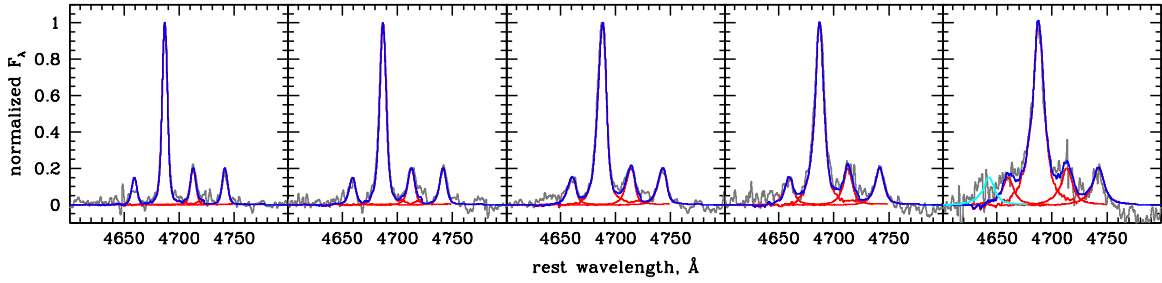


FIG. 14.— Zoom in on the wavelength region that may contain Wolf-Rayet signatures for the five composite spectra made in bins of [OIII] line width, which is increasing from left to right. In each panel, the grey histogram shows the composite spectrum and the red curves show H β velocity profiles (from the same composite) scaled to match the amplitudes of [Fe III] λ 4658, He II λ 4686, [Ar IV] λ 4711 and [Ar IV] λ 4740. In all five panels, [Fe III]/He II=0.15 and each [Ar IV]/He II=0.2. The blue curve shows the sum of the red profiles. The light blue curve in the last panel shows the putative N III λ 4640 component.

(1999) to estimate star-formation rates of $\sim 6 M_{\odot}/\text{year}$. This is significantly lower than the estimates of star formation rates in type 2 quasar hosts by Zakamska et al. (2008) (a few tens M_{\odot}/year). The difference between the two methods is not alarming because there are still significant discrepancies between modeled and observed fluxes of Wolf-Rayet features, especially as a function of metallicity (Brinchmann et al. 2008). But the low fluxes of Wolf-Rayet features in our composites – if they are detected at all – further reinforce our understanding that the star formation rates in type 2 quasar hosts are not adequate for producing the observed radio emission. At $10 M_{\odot}/\text{year}$, using calibrations by Bell (2003) and Rosario et al. (2013) we find that typical star-forming galaxies would produce $\nu L_{\nu}[1.4\text{GHz}] = 2.5 \times 10^{38} \text{ erg/sec}$ and $\nu L_{\nu}[12\mu\text{m}] = 2.9 \times 10^{43} \text{ erg/sec}$, more than an order of magnitude below the values seen in our sample.

5.3. Line ratios as a function of line width and line luminosity

Figure 15 summarizes our analysis of the line ratios as a function of [OIII] width and luminosity. Among the most noticeable trends is a dramatic increase of [SII] $\lambda\lambda$ 4069,4076 (and to a lesser extent, [NI] $\lambda\lambda$ 5198,5200) as a function of [OIII] width, which is our proxy for outflow velocity. Line ratios that vary with kinematics are often a tell-tale sign of shock excitation in star-burst galaxies and LINERs (Veilleux et al. 1994, 1995). [SII] and [NI] trace warm weakly ionized gas phase, which is common in shocks that penetrate deep into clouds and that can produce extended low-ionization regions (Tielens 2005). The increase in the relative prominence of these lines suggests an increase in shock-ionization contribution, perhaps in direct response to an increase of the quasar wind velocity.

The [OIII] λ 4363/[OIII] λ 5007 ratio is $\simeq 1.7 \times 10^{-2}$ and does not vary in a regular fashion with either [OIII] width or luminosity. This value is significantly higher than that predicted by photo-ionization models (Villar-Martín et al. 2008), and is higher still if corrected for extinction. Combined shock- and photo-ionization models (Moy & Rocca-Volmerange 2002) can help explain this ratio, but because photo-ionization makes the dominant contribution to the [OIII] emission the lack of dependence on line kinematics is not too surprising.

Both [SII] $\lambda\lambda$ 4069,4076 and especially [NI] $\lambda\lambda$ 5198,5200

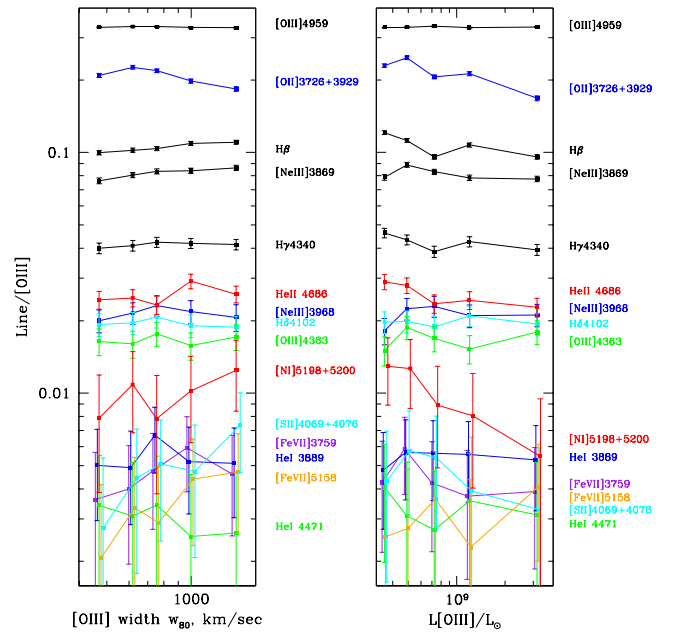


FIG. 15.— Line ratios as a function of line width (left) and [OIII] line luminosity (right) calculated from the composite spectra. On the horizontal axis, we use the median w_{80} (in km/sec) or the [OIII] line luminosity of the spectra contributing to the particular composite. Some curves are color-coded in no particular order to help distinguish them on the plot, and the bottom six curves are offset from each other by a small amount in the horizontal direction for the same reason; no actual change of line width or line luminosity is present.

decline strongly as a function of [OIII] luminosity. This suggests that the low-ionization regions are being destroyed as $L[\text{OIII}]$ increases, likely as a result of the increase in the bolometric luminosity and thus the availability of ionizing photons. The same effect could also be produced by the increase in the opening angle of quasar obscuration, which would increase the size of the photo-ionized regions and lead to obliteration of the low-ionization regions by direct quasar radiation, but the strong positive [OIII]-infrared correlation suggests that the bolometric luminosity increase is the more likely driver for the observed correlations.

The [OII]/[OIII] decrease as a function of lumi-

osity was previously reported by Kim et al. (2006), with our values being in agreement with theirs. Quasar photo-ionization produces poor fits to this ratio (Villar-Martín et al. 2008). Explanations usually involve a combination of high-ionization regions photo-ionized by the quasar and low-ionization regions photo-ionized by star formation (Kim et al. 2006), so the decrease in $[\text{OII}]/[\text{OIII}]$ with $[\text{OIII}]$ luminosity then indicates the decrease in the relative contribution of the lower-ionization regions, which is similar to the behavior of $[\text{SII}]$ and $[\text{NI}]$ lines. However, unlike $[\text{SII}]$ and $[\text{NI}]$, $[\text{OII}]/[\text{OIII}]$ decreases with $[\text{OIII}]$ line width. We speculate that this trend may be an indirect hint that the quasar-driven wind of increasing velocity (as measured by $[\text{OIII}]$ width) suppresses star formation in the host galaxy, a phenomenon which on occasion can be observed in action in individual sources (Cano-Díaz et al. 2012).

We do not find any noticeable trends in line ratios with radio luminosity, except that the lines are getting broader as the radio luminosity increases. This confirms our previous finding of the correlation between $[\text{OIII}]$ width and radio luminosity (Figure 10), but suggests that radio emission is not one of the principal drivers of the state of the ionized gas. Furthermore, there is no evidence that Wolf-Rayet features appear in higher radio luminosity objects, which is in qualitative agreement with our previous conclusion that radio emission is not dominated by the star formation in the host. We also examine composite spectra made in bins of infrared luminosity and find their behaviour similar to those made in bins of $[\text{OIII}]$ luminosity, except that the width of the lines is a significantly stronger function of infrared than $[\text{OIII}]$ luminosity, as we already know from Figures 10 and 11.

In the highest line width composite, the profile of $[\text{OII}]$ is visibly narrower than that of $[\text{OIII}]$, and indeed we find $w_{90}[\text{OIII}] = 2132$ km/sec ($w_{80} = 1498$ km/sec), whereas that of $[\text{OII}]$ (corrected for doublet structure using eq. 1) is 1410 km/sec (1040 km/sec). This confirms the trend we see in Figure 8 and may mean that the $[\text{OII}]/[\text{OIII}]$ ratios calculated from the composite spectra are overestimated (as they are computed with a fixed velocity profile of $[\text{OIII}]$). For any lines other than $[\text{OII}]$, even with the high S/N of the composite spectrum it is not clear whether the kinematic structures are consistent from one line to the next. There is a hint that $[\text{NI}]\lambda\lambda 5198, 5200$ is narrower than $[\text{OIII}]$ as well. We do not detect any obvious overall blueshifts of any features relative to $[\text{OIII}]$.

Another curious tidbit is the increase in the He I $\lambda 3889$ / He I $\lambda 4471$ ratio with $[\text{OIII}]$ width. This ratio ranges from 1.2 to 2.1, which is significantly lower than the standard Case B values (Osterbrock & Ferland 2006). If we correct them for the extinction, we find values in the range 1.8 to 2.6 (still somewhat lower than Case B) and increasing monotonically with w_{80} (in the last w_{80} He I $\lambda 3889$ /He I $\lambda 4471$ is likely underestimated because He I $\lambda 3889$ starts to blend with $[\text{NeIII}]\lambda 3869$), without any trend with $L[\text{OIII}]$. It is possible that He I is affected by self-absorption (Monreal-Ibero et al. 2013) which declines as a function of line width.

5.4. Coronal lines

We detect two very high-ionization features, $[\text{Fe VII}]\lambda 3759$ and $[\text{Fe VII}]\lambda 5158$, which show a tendency to

increase with $[\text{OIII}]$ width. Such lines, termed “coronal”, arise from ions with high ionization potential, 99 eV in the case of FeVII. The most frequently discussed mechanism for their production is excitation by quasar photo-ionization fairly close to the nucleus, akin to an “intermediate” region between the very compact broad-line region and a more extended narrow-line one (Grandi 1978; Gelbord et al. 2009; Mullaney et al. 2009; Müller-Sánchez et al. 2011). In photo-ionization models, high electron and photon densities are typically required to produce coronal lines, which explains why they arise close to the nucleus, e.g., at sub-pc scale in the case of a Seyfert galaxy modeled by Mullaney et al. (2009). These authors propose that the inner edge of the obscuring material is the plausible location of the coronal emission regions. Similarly, the rapid variability of coronal line emission in another Seyfert galaxy suggests that the size of the emission region is just a few light years (Komossa et al. 2008).

Such small distances present a challenge to the study by Rodríguez-Ardila et al. (2011) who find that the coronal lines are detected at similar rates in type 1 and type 2 objects, indicating that they originate outside the obscuring material, although Rodríguez-Ardila et al. (2011) still require very high densities, $n_e = 10^8 - 10^9$ cm $^{-3}$. If coronal lines originate somewhere near the inner edge of the obscuring material, depending on the orientation we may see them in an occasional type 2 object, but overall one would expect to see lower detection rates of coronal lines in type 2 objects than in type 1s in this scenario.

It would be surprising to see the a region close to or inside of the obscuring material in type 2 quasars, and even more surprising to see its flux correlate with the kinematics of much lower-ionization, much more extended gas. Therefore, we suggest that instead of circumnuclear photo-ionization in type 2 quasars some or most of the coronal lines are due to shocks, possibly those produced when the radiatively-accelerated wind from the quasar runs into dense clouds.

We draw inspiration from the observations by Mazzalay et al. (2013) who find that the extended ($\lesssim 170$ pc) coronal line emission in NGC 1068 is likely dominated by shock excitation. These authors find that coronal line ratios are more easily explained by shock models than by photo-ionization models. Furthermore, they find that the kinematic structure of coronal lines is similar to that of several lower ionization features. Most intriguingly, the spatial and kinematic distribution of coronal lines is similar to that of very low ionization lines, such as $[\text{FeII}]$, characteristic of shocks propagating into partly ionized medium. The latter point is particularly interesting as we observe the simultaneous rise of coronal lines and $[\text{SII}]$ and $[\text{NI}]$ in our sources.

In NGC 1068, coronal lines are co-spatial with the radio jet, and thus Mazzalay et al. (2013) suggest that jet-driven shocks may play a role in line excitation. This is also a possibility for our sources and for type 1 quasars (Husemann et al. 2013; Mullaney et al. 2013), especially in light of the fact that radio emission is strongly correlated with line kinematics (Section 4.1). However, we do not favor this scenario. While radio luminosity increases with $[\text{OIII}]$ widths, and so do the fluxes of $[\text{FeVII}]$, $[\text{SII}]$

and [NI], there is no evidence that the latter lines increase in the composites made in bins of radio luminosity. What this suggests to us is that the primary driver for all these correlations is not the power of the radio emission, but the kinematics of the gas. Higher outflow velocity implies higher velocities of shocks driven into dense clouds, which enhances coronal emission, while the radio emission follows as discussed in Section 6.1.

What sort of conditions would be required to produce coronal lines by driving low-density wind into high-density clouds? The typical shock velocities inside the shocked clouds implied by the observed coronal line ratios in NGC 1068 are $v_{\text{shock}} = 300 - 1000$ km/sec for cloud densities $n_{\text{cloud}} = 100 - 300 \text{ cm}^{-3}$ (Mazzalay et al. 2013). To produce the same values in our picture, the incident wind velocity must be even higher, $v_{\text{wind}} \sim v_{\text{shock}} \sqrt{n_{\text{cloud}}/n_{\text{wind}}}$, where n_{wind} is the much lower density of the volume-filling component of the wind, so the required v_{wind} can be several thousand km/sec. Such high velocities are not achievable at large distances in low-luminosity active galaxies, where the radiatively-driven wind would get quenched by the interaction with the interstellar medium, but could be typical of quasar-driven winds (Moe et al. 2009; Zubovas & King 2012; Faucher-Giguère & Quataert 2012) even on galaxy-wide scales (Arav et al. 2013; Liu et al. 2013b).

6. DISCUSSION

6.1. *The origin of the line kinematics / radio / infrared relationships*

The tantalizing relationship between radio and infrared luminosities and the [OIII] line kinematics may contain interesting clues about the structure and the driving mechanism of ionized gas outflows in quasars, but its interpretation is not straightforward. For quite some time, it was thought that the extended ionized gas around active galaxies was much more likely to be found around radio-loud objects than around radio-quiet ones (Stockton & MacKenty 1987). This was in line with theoretical ideas: powerful relativistic jets can inflate over-pressured cocoons which in turn sweep up galactic and inter-galactic medium plausibly resulting in narrow-line emission (Begelman & Cioffi 1989).

With more sensitive observations, extended ionized gas emission has now been detected around radio-loud and radio-quiet quasars alike, indicating that gas nebulae around both types have roughly similar sizes (Liu et al. 2013a,b, 2014). The major difference appears to be that the nebulae around radio-loud objects tend to be more disturbed (lumpy) or more elongated, whereas the nebulae around radio-quiet objects are smooth and featureless (Liu et al. 2013a).

The recent discovery of the relationship between gas kinematics and radio emission within the radio-quiet population goes to the heart of the origin of the outflows in the majority of quasars, as well as of the origin of radio-quiet emission itself. Within the last year, there have been several new results on these issues (Condon et al. 2013; Husemann et al. 2013; Mullaney et al. 2013).

One hypothesis is that in the radio-quiet objects the radio emission is due to a compact jet not resolved in the current radio observations which is driving the outflow

of ionized gas (Husemann et al. 2013; Mullaney et al. 2013). This is in line with the classical work on narrow-line kinematics by Veilleux (1991a,b,c) who found a correlation between [OIII] λ 5007 line width and radio luminosity within a sample of 16 nearby Seyfert galaxies. In these nearby objects, high-resolution radio observations sometimes reveal a strong relationship between the position angle and morphology of the radio emission and the ionized gas emission (Veilleux 1991c).

In sources where the jet and the ionized gas emission are aligned, it is tempting to postulate that radio jets are either driving the outflow or provide shock-ionization, making them responsible for the morphology and / or excitation of the ionized gas, which may provide some basis for the radio / kinematics correlation. However, there may be a certain bias in reporting only those objects where high-resolution radio observations reveal a jet, especially if its position angle is not far off the orientation of the line emission. Not every source shows evidence of jets in high-resolution radio observations (Veilleux 1991c). In large unbiased samples the alignment between jets and ionized gas is statistically weak at best (Privon et al. 2008), although some authors find a stronger relationship (Schmitt et al. 2003), especially in compact radio sources (Shih et al. 2013). This remains a difficult issue because the morphology and the position angle of the radio emission and the ionized gas emission are a function of scale, and it is unclear which scales are relevant.

We examined 20 objects from our sample that are located in Stripe 82 and were mapped by the VLA by Hodge et al. (2011). These observations are deeper than FIRST (rms = $52 \mu\text{Jy/beam}$ vs $130 \mu\text{Jy/beam}$) and have higher spatial resolution (FWHM = $1.8''$ vs $5''$), better matched to the sizes of the quasar host galaxies at the typical redshifts of our sample ($1''$ at $z = 0.5$ is 6.1 kpc). Of the 20 sources, one object is a giant FR II radio galaxy in both datasets; 13 are point sources both in FIRST and in Stripe 82; and the remaining 7 are not detected in FIRST, but are all detected in Stripe 82 as point sources with fluxes between 0.4-0.7 mJy, i.e., just a factor of a couple below the catalog limit of the FIRST survey. None of the 19 objects showed resolved morphology in the higher resolution observations, although these observations would not be able to identify compact ($\lesssim 5$ kpc) jets.

A completely different approach is followed by Condon et al. (2013) who argue, on the basis of the shape of the radio luminosity function, that the radio emission in radio-quiet quasars is mostly or entirely due to star formation in their host galaxies. In our objects, in favor of this hypothesis is the strong correlation between the infrared and the radio fluxes, which furthermore appear to lie on the extension of the locus of normal star-forming galaxies (Figure 11). However, at the luminosity of the radio-quiet subsample of $\log(\nu L_{\nu}[1.4\text{GHz}], \text{erg/sec}) = 40.0 \pm 0.7$ (mean=median and standard deviation), the median star formation rate suggested by the classical radio / star-formation correlation (Helou et al. 1985; Bell 2003) would be an astonishing $400 M_{\odot}/\text{year}$. Although the star formation rates of type 2 quasar hosts are among the highest in the population of active galaxies, in the ballpark of a few tens M_{\odot}/year (Zakamska et al. 2008), they fall short of the values required to explain the observed radio lumi-

osity. Furthermore, as was already noted above, the mid-infrared fluxes of our objects shown in Figure 11 are dominated by the emission of the quasar-heated dust. Thus both radio luminosity and mid-infrared luminosity in Figure 11 are unlikely to be due to star formation.

We propose instead that the shock blast initiated by the quasar feedback accelerates particles, just like what happens in a supernova remnant, which then produce synchrotron emission (Jiang et al. 2010; Faucher-Giguère & Quataert 2012; Zubovas & King 2012). To estimate the energetics of the wind required in this scenario, we assume for the moment that the efficiency of converting the kinetic energy of the outflow L_{wind} into radio synchrotron emission is similar in starburst-driven and quasar-driven winds. In a galaxy forming $\psi M_{\odot}/\text{year}$ worth of stars, the kinetic energy of the starburst-driven wind is $7 \times 10^{41} \psi$ erg/sec (Leitherer et al. 1999). The same galaxy produces $\nu L_{\nu}[1.4\text{GHz}] = 2.5 \times 10^{37} \psi$ erg/sec worth of radio emission (Bell 2003), with efficiency of 3.6×10^{-5} of converting kinetic energy into radio luminosity.

Applying the same efficiency to our objects, we find that to reproduce our median radio luminosity of 10^{40} erg/sec we need $L_{\text{wind}} = 3 \times 10^{44}$ erg/sec. The bolometric luminosities of our objects are poorly known, but using scalings presented by Liu et al. (2009) we can estimate that for the median [OIII] luminosity of our sample ($\log L[\text{OIII}]/L_{\odot} = 8.9$) the bolometric luminosity is 8×10^{45} erg/sec. Thus the median fraction of the bolometric luminosity converted to the kinetic luminosity of the wind is 4%, in rough agreement with our previous estimates based on observations of spatially resolved winds (Liu et al. 2013b). These ideas are further supported by our observation that $\nu L_{\nu}[1.4\text{GHz}]$ has a close-to-quadratic dependence on [OIII] width (Figure 10), suggesting that the relationship between the kinetic energy of the ionized gas and radio luminosity is linear.

6.2. Radiatively-driven quasar winds

In Figure 16 we present a schematic of the components of the narrow-line regions of quasars discussed in this paper. The quasar is in the center and is characterized by its bolometric luminosity L_{bol} . Obscuring material is distributed anisotropically around it (dark grey “torus”), with Ω being the opening angle of the obscuration which determines the directions that can be photo-ionized by the direct quasar radiation. The relationship between the two values L_{bol} and Ω is not well known. Demographic studies of quasars continue to disagree on whether the obscured fraction stays constant or decreases as a function of luminosity (Treister et al. 2008; Lawrence & Elvis 2010), but it is likely that at a given luminosity there is a wide distribution of Ω (Zakamska et al. 2006).

Another component of the model is the quasar-driven wind. The wind may be initially driven anisotropically, e.g., close to the equatorial plane of the accretion disk (Murray et al. 1995; Proga et al. 2000), and when it is first launched near the quasar, it is very fast, with velocities up to $\sim 0.1c$. The wind runs into the interstellar medium close to the nucleus and interacts with it, producing shock waves that propagate through the interstellar medium of the galaxy. If this medium is clumpy, the propagation of the wind proceeds along paths of least

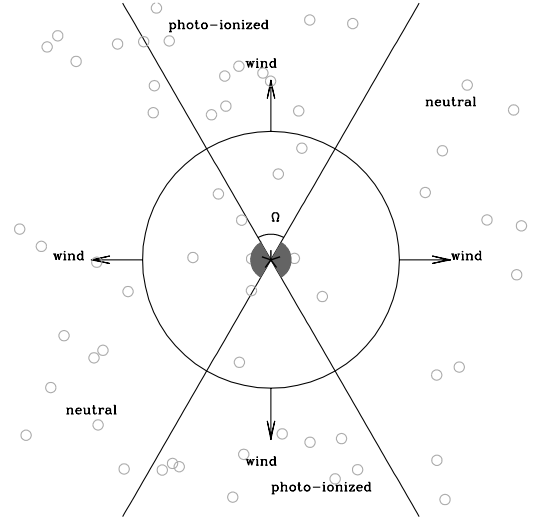


FIG. 16.— A cartoon of our model for the narrow-line region of a quasar (central 5-point star). The quasar is surrounded by circumnuclear obscuring material (dark grey “torus”) whose opening angle is Ω . The wind propagates more isotropically than the ionizing radiation from the quasar which is concentrated in bi-cones marked “photo-ionized”. Optical emission lines are produced by dense clouds (small circles).

resistance, and the shape of the large-scale wind is determined largely by the distribution of the interstellar medium (Wagner et al. 2013), rather than by the initial anisotropies. Thus the wind is shown propagating in all directions, even those that are affected by the circumnuclear obscuration.

The wind velocity v_{wind} likely varies as a function of the location in the galaxy and is not well-known observationally. In our data, the line-of-sight velocity dispersion of the optical emission lines is characteristic of the velocities of the clouds v_0 (light grey), not the velocity of the wind. The acceleration of clouds and their survival as they are impacted by the wind is a topic of active research (Mellema et al. 2002; Cooper et al. 2009; Alūzas et al. 2012; Barai et al. 2012; Faucher-Giguère et al. 2012), but it seems natural that the velocity of the wind should be at least as high as the velocity of the clouds that it accelerates ($v_{\text{wind}} \gtrsim v_0$) and that they should be strongly related. Theoretical arguments suggest wind velocities of $v_{\text{wind}} \gtrsim 1000$ km/sec (King 2005; Zubovas & King 2012; Faucher-Giguère & Quataert 2012), in rough agreement with our inferred values of v_0 .

We do not observe v_0 directly; rather, we infer these values from the line-of-sight velocity width of the emission lines. The increase in shock-diagnostic lines [SII], [NI] and possibly [FeVII] as a function of [OIII] width provides strong evidence that the observed velocity width is a good proxy for the outflow velocity. Furthermore, the [OIII] width positively correlates with mid-infrared luminosity (Figure 11), which we take to suggest that the outflow is ultimately driven by the radiative pressure near the quasar (Murray et al. 1995; Proga et al. 2000). After the winds are launched, they interact with the interstellar medium in complex ways, which perhaps explains why the correlation between infrared luminosity

and [OIII] velocity width (which our observations probe on galaxy-wide scales, Liu et al. 2013b) has a large scatter.

7. CONCLUSIONS

7.1. Gas kinematics and outflows

In this paper we study the kinematics of ionized gas emission in 568 luminous obscured quasars from the sample of Reyes et al. (2008), primarily using their [OIII] $\lambda\lambda 4959, 5007$ emission lines. For every object, we determine a set of non-parametric measures of line asymmetry, velocity width and shape. We find that objects with blue-shifted emission and line asymmetries are more prevalent in our sample, which we take as a signature that outflows in which the redshifted part is affected by dust extinction are common in our sample. The velocity widths we see in our sample (median $w_{80} = 752$ km/sec and $w_{90} = 1060$ km/sec, max $w_{80} = 2918$ km/sec and $w_{90} = 4780$ km/sec) are much higher than those in starburst galaxies (median $w_{90} \simeq 600$ km/sec, Rupke & Veilleux 2013; Hill & Zakamska 2013).

Using the conversion between the line-of-sight velocity width of the line and the outflow velocity from Section 3.1, we can estimate outflow velocities as $v_0 \simeq w_{80}/1.5$. We find that for about half of the objects in our sample, v_0 ranges from ~ 500 to ~ 2000 km/sec. It is likely that in every object a range of cloud velocities is present; these estimates should be thought of as the median velocities in each source. From the observations presented here, it is not known which spatial scales dominate these estimates, but from our spatially resolved observations (Liu et al. 2013b) it is clear that at least some of the clouds maintain similar velocities all the way out to ~ 10 kpc from the quasar.

Neither the overall width, nor the width of the narrower component in the multi-Gaussian line decomposition correlate with the velocity dispersion of the host galaxy. We therefore find no evidence for significant amounts of gas in dynamical equilibrium with the host (e.g., a component associated with the rotating galaxy disk). The higher velocity gas tends to be on average blueshifted by ~ 100 km/sec relative to the lower velocity gas. This may mean that the higher velocity gas is found on somewhat smaller spatial scales which are more prone to dust extinction. This conclusion is in line with the slight observed decrease of line-of-sight velocity dispersions of the gas as a function of the distance from the nucleus seen in spatially resolved observations of quasar winds (Liu et al. 2013b). The effect is very subtle (3% decrease per each projected kpc), and overall high gas velocities are maintained over the entire host galaxy (Liu et al. 2013b). Other strong lines, such as [OII] and H β , also show outflow signatures, but significantly more mild than those seen in the [OIII] line. In the objects with the most extreme [OIII] kinematics, [OII] is much narrower than [OIII], with the kinematics of H β being in between the two.

The increase in shock-diagnostic lines [SII] $\lambda\lambda 4069, 4076$ and [NI] $\lambda\lambda 5198, 5200$ as a function of [OIII] width provides strong support for using the [OIII] width as a proxy for the outflow velocity. [OII] declines both with [OIII] width and [OIII] luminosity, suggesting that the [OII]-emitting regions are over-ionized by photo-ionization and

quenched by increasing shock velocity. We find evidence for shock-ionization contribution to coronal lines [FeVII].

7.2. Outflows and radio emission

[OIII] velocity width correlates strongly with radio luminosity. We suggest that the radio emission is a by-product of the outflow activity, with particles accelerated on the shock fronts as the radiatively driven quasar wind propagates into the interstellar medium of the host galaxy. The median radio luminosity in our sample, $\nu L_\nu[1.4\text{GHz}] = 10^{40}$ erg/sec, requires kinetic energy of the outflow of $L_{\text{wind}} = 3 \times 10^{44}$ erg/sec if the efficiency of conversion in quasar-driven winds is similar to that in supernova-driven winds. The bolometric luminosities of our objects are poorly known, but we estimate that the median value for our sample is 8×10^{45} erg/sec and thus the kinetic luminosity of the wind is 4% of the bolometric power. This idea is further reinforced by the approximately quadratic dependence $\nu L_\nu[1.4\text{GHz}] \propto (\text{width}[\text{OIII}])^2$, which implies a linear relationship between radio luminosity and kinetic energy of the outflow. [OIII] velocity is positively correlated with the infrared luminosity, which suggests that the ionized gas outflow is ultimately driven by the radiative pressure close to the accreting black hole.

Another possible explanation for the [OIII] width / radio correlation is that the mechanical energy of the relativistic jet (which has not yet broken out of its host galaxy) is used to heat an overpressured cocoon (Begelman & Cioffi 1989) which then launches the wind of ionized gas (Mullaney et al. 2013). As long as the jet is still compact, it appears as an unresolved radio core in FIRST observations. We use the scalings between the core radio luminosity and the jet kinetic energy by Merloni & Heinz (2007) to estimate how much kinetic power would be required to produce the observed median radio luminosity. We find $L_{\text{jet}} = 3 \times 10^{44}$ erg/sec, a value which is almost identical to the wind kinetic power obtained in the previous paragraph, even though they were estimated using completely different methods. This is likely not a coincidence: the efficiency of conversion of mechanical luminosity into synchrotron radiation is determined by the fraction of energy that can be converted into relativistic particles on shock fronts, which is likely independent of the origin of these shocks.

The similarity of energy requirements underscores the difficulty of distinguishing between these two mechanisms. In the jet scenario one expects to see a jet in the high-resolution radio observations, whereas in the wind scenario radio emission is more diffuse and is present everywhere where shocks are propagating; however, in practice the collimated part of the jet does not dissipate energy very efficiently and so can be hard to detect. In both models, the morphology of the ionized gas depends much more strongly on the distribution of the interstellar medium than on the exact driving mechanism (Gaibler et al. 2011; Wagner et al. 2012, 2013). Thus, the morphology of ionized gas is not necessarily a useful clue.

Radio spectral index could be a useful measurement for identifying recent or on-going particle acceleration (flatter synchrotron spectra for freshly accelerated, more energetic particles), but again particle acceleration may be happening in both scenarios. Interestingly, Lal & Ho

(2010) find flatter spectral indices in type 2 quasars than expected for jets in the standard geometry-based unification models, so a combination of spectral and morphological investigations in the radio may be worth pursuing further.

One uncomfortable consequence of the jet scenario is that it requires for every radio-quiet quasar to have a powerful jet, with only a minority of them being active long enough to break out of the galaxy (otherwise there would be too many extended radio sources). Another problem is that the jet scenario provides no ready explanation for the correlation between [OIII] width and infrared luminosity.

In the wind scenario, if the initial distribution of matter is roughly spherically symmetric, so will be the ionized gas emission and the radio emission. In a disk galaxy, once the size of the wind reaches the vertical scaleheight of the disk it propagates largely along the path of least resistance perpendicular to the disk (Wagner et al. 2013), forming two symmetric bubbles on either side. Ionized gas emission is concentrated in shells and filaments, whereas the radio emission is filling the bubbles. In low-resolution data, one would see both the line emission and the radio emission oriented roughly in the same direction, so distinguishing this mechanism from jet-induced outflow requires high-quality observations.

Such bubbles are directly seen in the radio in external galaxies (Cecil et al. 2001; Hota & Saikia 2006) and in our own Milky Way, where the bubbles are known as “the microwave haze” (Finkbeiner 2004; Su et al. 2010). These structures are also seen in X-rays which often closely trace the morphology of the radio emission and / or the ionized gas filaments (Cecil et al. 2001; Croston et al. 2008; Wang et al. 2009). In our Galaxy not only X-rays are observed (Sofue 2000), but the structures as seen in gamma-rays and are known as “the Fermi bubbles” (Su et al. 2010). For comparison, the mechanical luminosity necessary to inflate the bubbles in NGC

3079 (Cecil et al. 2001) is ~ 30 lower than our median L_{wind} , whereas that inferred for “the Fermi bubbles” in the Milky Way is 10^5 times lower than our L_{wind} . It is interesting that all of the examples above host jets (Cecil et al. 2001; Croston et al. 2008; Wang et al. 2009; Su & Finkbeiner 2012), but it remains unclear whether this is universally true and whether they are contributing most of the required power.

7.3. Feedback in low- and high-luminosity active galaxies

Our investigation focuses on the most luminous type 2 quasars at $z \lesssim 1$. In these sources, we find strong evidence for quasar-driven winds on galaxy-wide scales, for radio emission associated with these winds, and for ionized gas velocities in excess of escape velocity from the galaxy. In lower luminosity active galaxies, many previous studies demonstrated that ionized gas is in dynamical equilibrium with the host galaxy and that radio emission is likely a bi-product of star-formation processes. Thus quasar-driven feedback may be present above some threshold in luminosity and absent below this threshold. We estimate this threshold by observing that in Figure 11, our sources separate well from star-forming galaxies at about $\nu L_\nu[12\mu\text{m}] = 2 \times 10^{44}$ erg/sec. Using bolometric corrections from Richards et al. (2006), Liu et al. (2009) and Liu et al. (2013b), we estimate the corresponding bolometric luminosity to be $L_{\text{bol}} = 3 \times 10^{45}$ erg/sec (uncertainty ± 0.4 dex).

NLZ would like to acknowledge useful conversations with M.J.Collinge (who suggested the diffuse nature of radio emission) and S.Tremaine (who suggested the analogy with Fermi bubbles), as well as with B.Groves, J.Krolik and D.Kushnir. NLZ is thankful for the continued hospitality of the Institute for Advanced Study (Princeton) where part of this work was performed.

REFERENCES

- Alūzas, R., Pittard, J. M., Hartquist, T. W., Falle, S. A. E. G., & Langton, R. 2012, MNRAS, 425, 2212
- Alexander, D. M., Swinbank, A. M., Smail, I., McDermid, R., & Nesvadba, N. P. H. 2010, MNRAS, 402, 2211
- Antonucci, R. R. J., & Miller, J. S. 1985, ApJ, 297, 621
- Arav, N., Borguet, B., Chamberlain, C., Edmonds, D., & Danforth, C. 2013, MNRAS, 436, 3286
- Arav, N., Moe, M., Costantini, E., et al. 2008, ApJ, 681, 954
- Barai, P., Proga, D., & Nagamine, K. 2012, MNRAS, 424, 728
- Barrows, R. S., Sandberg Lacy, C. H., Kenefick, J., et al. 2013, ApJ, 769, 95
- Becker, R. H., White, R. L., & Helfand, D. J. 1995, ApJ, 450, 559
- Begelman, M. C., & Cioffi, D. F. 1989, ApJ, 345, L21
- Bell, E. F. 2003, ApJ, 586, 794
- Bennert, N., Jungwiert, B., Komossa, S., Haas, M., & Chini, R. 2006, A&A, 456, 953
- Blecha, L., Loeb, A., & Narayan, R. 2013, MNRAS, 429, 2594
- Brinchmann, J., Kunth, D., & Durret, F. 2008, A&A, 485, 657
- Bruzual, G., & Charlot, S. 2003, MNRAS, 344, 1000
- Cano-Díaz, M., Maiolino, R., Marconi, A., et al. 2012, A&A, 537, L8
- Cecil, G., Bland-Hawthorn, J., Veilleux, S., & Filippenko, A. V. 2001, ApJ, 555, 338
- Comerford, J. M., et al. 2009, ApJ, 698, 956
- Condon, J. J., Cotton, W. D., Greisen, E. W., et al. 1998, AJ, 115, 1693
- Condon, J. J., Kellermann, K. I., Kimball, A. E., Ivezić, Ž., & Perley, R. A. 2013, ApJ, 768, 37
- Cooper, J. L., Bicknell, G. V., Sutherland, R. S., & Bland-Hawthorn, J. 2009, ApJ, 703, 330
- Crenshaw, D. M., & Kraemer, S. B. 2000, ApJ, 532, L101
- Crenshaw, D. M., Kraemer, S. B., & George, I. M. 2003, ARA&A, 41, 117
- Croston, J. H., Hardcastle, M. J., Kharb, P., Kraft, R. P., & Hota, A. 2008, ApJ, 688, 190
- De Robertis, M. M., & Osterbrock, D. E. 1984, ApJ, 286, 171
- Dunn, J. P., Bautista, M., Arav, N., et al. 2010, ApJ, 709, 611
- Faucher-Giguère, C.-A., & Quataert, E. 2012, MNRAS, 425, 605
- Faucher-Giguère, C.-A., Quataert, E., & Murray, N. 2012, MNRAS, 420, 1347
- Finkbeiner, D. P. 2004, ApJ, 614, 186
- Fu, H., Yan, L., Myers, A. D., et al. 2012, ApJ, 745, 67
- Gaibler, V., Khochfar, S., & Krause, M. 2011, MNRAS, 411, 155
- Gelbord, J. M., Mullaney, J. R., & Ward, M. J. 2009, MNRAS, 397, 172
- Grandi, S. A. 1978, ApJ, 221, 501
- Greene, J. E., & Ho, L. C. 2005, ApJ, 627, 721
- . 2006, ApJ, 641, 117
- Greene, J. E., Zakamska, N. L., Ho, L. C., & Barth, A. J. 2011, ApJ, 732, 9
- Greene, J. E., Zakamska, N. L., Liu, X., Barth, A. J., & Ho, L. C. 2009, ApJ, 702, 441
- Greene, J. E., Zakamska, N. L., & Smith, P. S. 2012, ApJ, 746, 86

- Hainline, K. N., Hickox, R., Greene, J. E., Myers, A. D., & Zakamska, N. L. 2013, submitted
- Harrison, C. M., Alexander, D. M., Swinbank, A. M., et al. 2012, *MNRAS*, 426, 1073
- Heckman, T. M., Miley, G. K., van Breugel, W. J. M., & Butcher, H. R. 1981, *ApJ*, 247, 403
- Helou, G., Soifer, B. T., & Rowan-Robinson, M. 1985, *ApJ*, 298, L7
- Hill, M. J., & Zakamska, N. L. 2013, ArXiv:1311.0311
- Hodge, J. A., Becker, R. H., White, R. L., Richards, G. T., & Zeimann, G. R. 2011, *AJ*, 142, 3
- Hopkins, P. F., Hernquist, L., Cox, T. J., et al. 2006, *ApJS*, 163, 1
- Hota, A., & Saikia, D. J. 2006, *MNRAS*, 371, 945
- Husemann, B., Wisotzki, L., Sánchez, S. F., & Jahnke, K. 2013, *A&A*, 549, A43
- Ivezić, Z., Menou, K., Knapp, G. R., et al. 2002, *AJ*, 124, 2364
- Jia, J., Ptak, A., Heckman, T., & Zakamska, N. 2012, ArXiv e-prints
- Jiang, L., Fan, X., Ivezić, Ž., et al. 2007, *ApJ*, 656, 680
- Jiang, Y.-F., Ciotti, L., Ostriker, J. P., & Spitkovsky, A. 2010, *ApJ*, 711, 125
- Kellermann, K. I., Sramek, R., Schmidt, M., Shaffer, D. B., & Green, R. 1989, *AJ*, 98, 1195
- Kim, M., Ho, L. C., & Im, M. 2006, *ApJ*, 642, 702
- King, A. 2005, *ApJ*, 635, L121
- Komossa, S., Zhou, H., Wang, T., et al. 2008, *ApJ*, 678, L13
- Kramida, A., Yu. Ralchenko, Reader, J., & and NIST ASD Team. 2013, NIST Atomic Spectra Database (ver. 5.1), [Online]. Available: <http://physics.nist.gov/asd> [2014, January 2]. National Institute of Standards and Technology, Gaithersburg, MD.
- Lacy, M., Storrie-Lombardi, L. J., Sajina, A., et al. 2004, *ApJS*, 154, 166
- Lacy, M., Ridgway, S. E., Gates, E. L., et al. 2013, *ApJS*, 208, 24
- Lal, D. V., & Ho, L. C. 2010, *AJ*, 139, 1089
- Lawrence, A., & Elvis, M. 2010, *ApJ*, 714, 561
- Leitherer, C., Schaerer, D., Goldader, J. D., et al. 1999, *ApJS*, 123, 3
- Liu, G., Zakamska, N. L., & Greene, J. E. 2014, ArXiv e-prints
- Liu, G., Zakamska, N. L., Greene, J. E., Nesvadba, N. P. H., & Liu, X. 2013a, *MNRAS*, 430, 2327
- , 2013b, *MNRAS*, 436, 2576
- Liu, X., Shen, Y., Strauss, M. A., & Greene, J. E. 2010, *ApJ*, 708, 427
- Liu, X., Zakamska, N. L., Greene, J. E., et al. 2009, *ApJ*, 702, 1098
- Mazzalay, X., Rodríguez-Ardila, A., Komossa, S., & McGregor, P. J. 2013, *MNRAS*, 430, 2411
- Mellema, G., Kurk, J. D., & Röttgering, H. J. A. 2002, *A&A*, 395, L13
- Merloni, A., & Heinz, S. 2007, *MNRAS*, 381, 589
- Moe, M., Arav, N., Bautista, M. A., & Korista, K. T. 2009, *ApJ*, 706, 525
- Monreal-Ibero, A., Walsh, J. R., Westmoquette, M. S., & Vílchez, J. M. 2013, *A&A*, 553, A57
- Morton, D. C. 1991, *ApJS*, 77, 119
- Moy, E., & Rocca-Volmerange, B. 2002, *A&A*, 383, 46
- Mullaney, J. R., Alexander, D. M., Fine, S., et al. 2013, *MNRAS*, 433, 622
- Mullaney, J. R., Ward, M. J., Done, C., Ferland, G. J., & Schurch, N. 2009, *MNRAS*, 394, L16
- Müller-Sánchez, F., Prieto, M. A., Hicks, E. K. S., et al. 2011, *ApJ*, 739, 69
- Murray, N., Chiang, J., Grossman, S. A., & Voit, G. M. 1995, *ApJ*, 451, 498
- Nelson, C. H., & Whittle, M. 1996, *ApJ*, 465, 96
- Nesvadba, N. P. H., Lehnert, M. D., De Breuck, C., Gilbert, A. M., & van Breugel, W. 2008, *A&A*, 491, 407
- Nesvadba, N. P. H., Lehnert, M. D., Eisenhauer, F., et al. 2006, *ApJ*, 650, 693
- Novak, G. S., Ostriker, J. P., & Ciotti, L. 2011, *ApJ*, 737, 26
- Osterbrock, D. E., & Ferland, G. J. 2006, *Astrophysics of gaseous nebulae and active galactic nuclei* (Sausalito, CA: University Science Books)
- Privon, G. C., O’Dea, C. P., Baum, S. A., et al. 2008, *ApJS*, 175, 423
- Proga, D., Stone, J. M., & Kallman, T. R. 2000, *ApJ*, 543, 686
- Ptak, A., Zakamska, N. L., Strauss, M. A., et al. 2006, *ApJ*, 637, 147
- Reyes, R., Zakamska, N. L., Strauss, M. A., et al. 2008, *AJ*, 136, 2373
- Richards, G. T., Lacy, M., Storrie-Lombardi, L. J., et al. 2006, *ApJS*, 166, 470
- Rodríguez-Ardila, A., Prieto, M. A., Portilla, J. G., & Tejeiro, J. M. 2011, *ApJ*, 743, 100
- Rosario, D. J., Bartscher, L., Davies, R., et al. 2013, *ApJ*, 778, 94
- Rupke, D. S. N., & Veilleux, S. 2013, *ApJ*, 768, 75
- Schaerer, D., Contini, T., & Kunth, D. 1999, *A&A*, 341, 399
- Schmitt, H. R., Donley, J. L., Antonucci, R. R. J., et al. 2003, *ApJ*, 597, 768
- Shen, Y., Liu, X., Greene, J., & Strauss, M. 2010, *ApJ*, submitted (astro/1011.5246)
- Shih, H.-Y., Stockton, A., & Kewley, L. 2013, *ApJ*, 772, 138
- Silk, J., & Rees, M. J. 1998, *A&A*, 331, L1
- Sofue, Y. 2000, *ApJ*, 540, 224
- Springel, V., Di Matteo, T., & Hernquist, L. 2005, *MNRAS*, 361, 776
- Stern, D., Eisenhardt, P., Gorjian, V., et al. 2005, *ApJ*, 631, 163
- Stockton, A., & MacKenty, J. W. 1987, *ApJ*, 316, 584
- Su, M., & Finkbeiner, D. P. 2012, *ApJ*, 753, 61
- Su, M., Slatyer, T. R., & Finkbeiner, D. P. 2010, *ApJ*, 724, 1044
- Tabor, G., & Binney, J. 1993, *MNRAS*, 263, 323
- Tielens, A. G. G. M. 2005, *The Physics and Chemistry of the Interstellar Medium*
- Treister, E., Krolik, J. H., & Dullemond, C. 2008, *ApJ*, 679, 140
- Vanden Berk, D. E., Richards, G. T., Bauer, A., et al. 2001, *AJ*, 122, 549
- Veilleux, S. 1991a, *ApJS*, 75, 357
- , 1991b, *ApJS*, 75, 383
- , 1991c, *ApJ*, 369, 331
- Veilleux, S., Cecil, G., Bland-Hawthorn, J., et al. 1994, *ApJ*, 433, 48
- Veilleux, S., Kim, D.-C., Sanders, D. B., Mazzarella, J. M., & Soifer, B. T. 1995, *ApJS*, 98, 171
- Vignali, C., Alexander, D. M., Gilli, R., & Pozzi, F. 2010, *MNRAS*, 404, 48
- Villar-Martín, M., Humphrey, A., Martínez-Sansigre, A., et al. 2008, *MNRAS*, 390, 218
- Wagner, A. Y., Bicknell, G. V., & Umemura, M. 2012, *ApJ*, 757, 136
- Wagner, A. Y., Umemura, M., & Bicknell, G. V. 2013, *ApJ*, 763, L18
- Wang, J., Fabbiano, G., Elvis, M., et al. 2009, *ApJ*, 694, 718
- Weingartner, J. C., & Draine, B. T. 2001, *ApJ*, 548, 296
- Whittle, M. 1985a, *MNRAS*, 213, 1
- , 1985b, *MNRAS*, 216, 817
- , 1992, *ApJ*, 387, 109
- Wilson, A. S., & Heckman, T. M. 1985, in *Astrophysics of Active Galaxies and Quasi-Stellar Objects*, ed. J. S. Miller, 39–109
- Xu, C., Livio, M., & Baum, S. 1999, *AJ*, 118, 1169
- York, D. G., et al. 2000, *AJ*, 120, 1579
- Zakamska, N. L., Gómez, L., Strauss, M. A., & Krolik, J. H. 2008, *AJ*, 136, 1607
- Zakamska, N. L., Strauss, M. A., Heckman, T. M., Ivezić, Ž., & Krolik, J. H. 2004, *AJ*, 128, 1002
- Zakamska, N. L., et al. 2003, *AJ*, 126, 2125
- , 2005, *AJ*, 129, 1212
- , 2006, *AJ*, 132, 1496
- Zubovas, K., & King, A. 2012, *ApJ*, 745, L34